

Martin Seiler, BSc

**Enhanced porosity in zinc oxide  
via  
molecular layer deposition**

**MASTER'S THESIS**

to achieve the university degree of  
Diplom-Ingenieur

Master's degree programme:  
Advanced Materials science

submitted to

**Graz University of Technology**

**Supervisor**

Assoc. Prof. Dr. Anna Maria Coclite

Institute for Solid State Physics

Graz, July 2020

## **AFFIDAVIT**

I declare that I have authored this thesis independently, that I have not used other than the declared sources/resources, and that I have explicitly indicated all material which has been quoted either literally or by content from the sources used. The text document uploaded to TUGRAZonline is identical to the present master's thesis.

---

Date, Signature

## **Acknowledgments**

---

First of all I want to thank my two supervisors Anna Coclite and Alberto Perrotta for their patient support and motivating guidance throughout this thesis.

I am very thankful for all the help I got from Anna Coclites research group. Especially I want to thank Richard Berger for introducing me into the topic and giving me advices whenever I needed them. Also I want to thank the other members of the group: Fabian Muralter, Marianne Kräuter, Julian Pilz, Katrin Unger and Taher Abu Ali for their support in the laboratory.

I want to thank Harald Kerschbaumer for all the technical support.

Furthermore I want to thank my friends who helped me to forget the days where nothing worked out and my girlfriend who had to endure me when I was frustrated.

Last but not least I want to thank my family for supporting me throughout the whole studies.



1	Introduction .....	1
2	Fundamentals.....	2
2.1	Molecular Layer Deposition .....	2
2.1.1	Introduction .....	2
2.1.2	Zincone Films.....	9
2.1.3	Porous Crystalline ZnO from Zincone Films .....	13
2.1.4	Photocatalytic Test .....	14
2.2	Characterization Methods.....	15
2.2.1	Fourier Transform Infrared Spectroscopy (FTIR) .....	15
2.2.2	X-Ray Diffraction (XRD).....	17
2.2.3	Spectroscopic Ellipsometry (SE) .....	18
2.2.4	Ellipsometric Porosimetry (EP).....	20
3	The MLD System.....	23
3.1	Reactor and Line Heating .....	24
3.2	Mass Flow Controller, Reactor Volume, Leak Rate.....	26
4	Experiments & Results.....	28
4.1	The Depositions .....	28
4.1.1	AB-depositions .....	29
4.1.2	ABC-depositions .....	32
4.2	Thin Film Characterisation.....	35
4.2.1	Heating Experiments .....	35
4.2.2	Plasma treatment of AB samples.....	42
4.2.3	Ellipsometric Porosimetry (EP).....	44
4.2.4	Photocatalytic test .....	51
4.2.5	Degradation .....	53
5	Summary and Conclusions.....	54
6	Device List .....	55
7	Figure List .....	56
8	Table List .....	58
9	Bibliography.....	59



# 1 INTRODUCTION

---

Zinc Oxide (ZnO) is a metaloxide material that is used in a wide range of applications due to its outstanding chemical and physical properties. It is a wide band gap semiconductor, transparent and the crystallization in the hexagonal wurtzite structure makes it piezoelectric. Transparent electronics, bio and UV sensors and varistors are only a few of the devices ZnO is used for. Studies show that in order to enhance the performance of this films even more a porous framework can be introduced [1]. For different applications different pore sizes can be favorable. For instance a uniform distribution of nanopores in ZnO enables it to detect cholesterol in blood veins [2]. Further examples are mesoporous films with pore sizes higher than 8 nm which enhance the photocatalytic performance of ZnO [3]. Macroporous films with an average pore size between 50 and 140 nm were tested in photoanodes and showed very promising results [4].

A major challenge for synthesizing porous ZnO is the conformal deposition on textured substrates. Most methods are limited to planar structures. Therefore the investigation of new synthesizing methods need to be studied.

A promising technique for the delivery of porous ZnO, which is able to deposit conformal even on nanostructures, is the molecular layer deposition (MLD). The MLD process depends on growing alternately single layers of zinc oxide and organic structures on a surface. This leads to the formation of a so called metal-organic hybrid film. After the desired amount of layers are deposited the organic content of the film is removed, for instance by heating, leaving behind voids in the structure. By varying the organic reactants or adding an additional one the size of the pores and the amount of open porosity can be easily tuned. This allows demand controlled production of differently porous ZnO structures.

## 2 FUNDAMENTALS

---

### 2.1 MOLECULAR LAYER DEPOSITION

#### 2.1.1 Introduction

Molecular layer deposition (MLD) is a process which promises the production of high quality thin films with control over the film thickness in the nanometer regime and great conformality even for complex three-dimensional structures. In MLD different gaseous precursors are introduced into a vacuum chamber at different times. Those precursors react at the surface of a substrate and build up layers. Between two precursor steps a purge step is introduced to ensure that always only one species is in the reaction chamber. In order to have a self-limiting process, the precursors are selected in a manner that they do not react with themselves but only with different precursor molecules. When all parameters are set optimal, one injection step is equal to one monolayer of the precursor added to the substrate. Thus, the film thickness can be controlled by the number of iterations. Although some literature can be found about three step MLD processes [5] most procedures are based on only two reactants.

Next to the synthesis of pure polymeric materials by using two or more organic ligands, hybrid organic-inorganic structures are achieved by combining those ligands with metalorganic precursors. The precursor variations exploited with MLD are rapidly increasing. In literature reported metal species cover the elements Al, Zn, Ti, Zr, Hf, V, Si, Fe and Mn. The resultant hybrid organic-inorganic film by combining metal precursors with various organic alcohols is often referred as “metalcone” [6]. Alucones are the most studied metalcones so far but also zincones, titanicones and zircones are found in literature.

By removing the organic part of the metal-alkoxide via wet-etching or annealing, porous metal oxide films can be achieved.

In this thesis the production of porous ZnO thin films by utilizing two and three step MLD processes following a calcination step is investigated. This production process is hereinafter referred to as AB process and ABC process. Starting from the reproduction of Zincone films, using the two precursors diethyl zinc (DEZ) and ethylene glycol (EG) as reported in a previous study by the TU Graz [7], a further metal-organic hybrid film was obtained. Therefore ethanolamine (EA) and maleic anhydride (MA) were applied as organic reactants and again DEZ provided the metallic part. The structural formulas of the different precursors are shown in Figure 1.



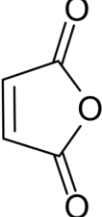
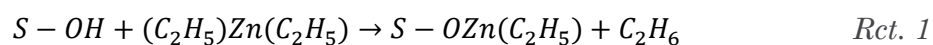
Diethylzinc (DEZ)	$\begin{array}{c} \text{H}_3\text{C} \\   \\ \text{H}_2\text{C}-\text{Zn}-\text{CH}_2 \\   \\ \text{CH}_3 \end{array}$	Ethanolamine (EA)	$\text{H}_2\text{N}-\text{CH}_2-\text{CH}_2-\text{OH}$
Ethylene glycol (EG)	$\text{HO}-\text{CH}_2-\text{CH}_2-\text{OH}$	Maleic anhydride (MA)	

Figure 1: Precursor structural formulas

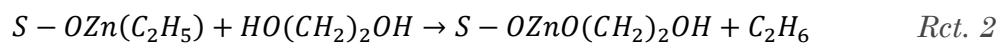
DEZ and EG both are homobifunctional reactants. They have the same reactive groups on both sides of the molecules, two ethyl groups for DEZ and two hydroxyl groups for EG. In the case of the ABC MLD process a heterobifunctional reactant EA and a ring-opening reactant MA are additionally employed to DEZ.

The surface reactions during the AB sequence and the associated schemes follow [7]:

(A)



(B)



S denotes the substrate.

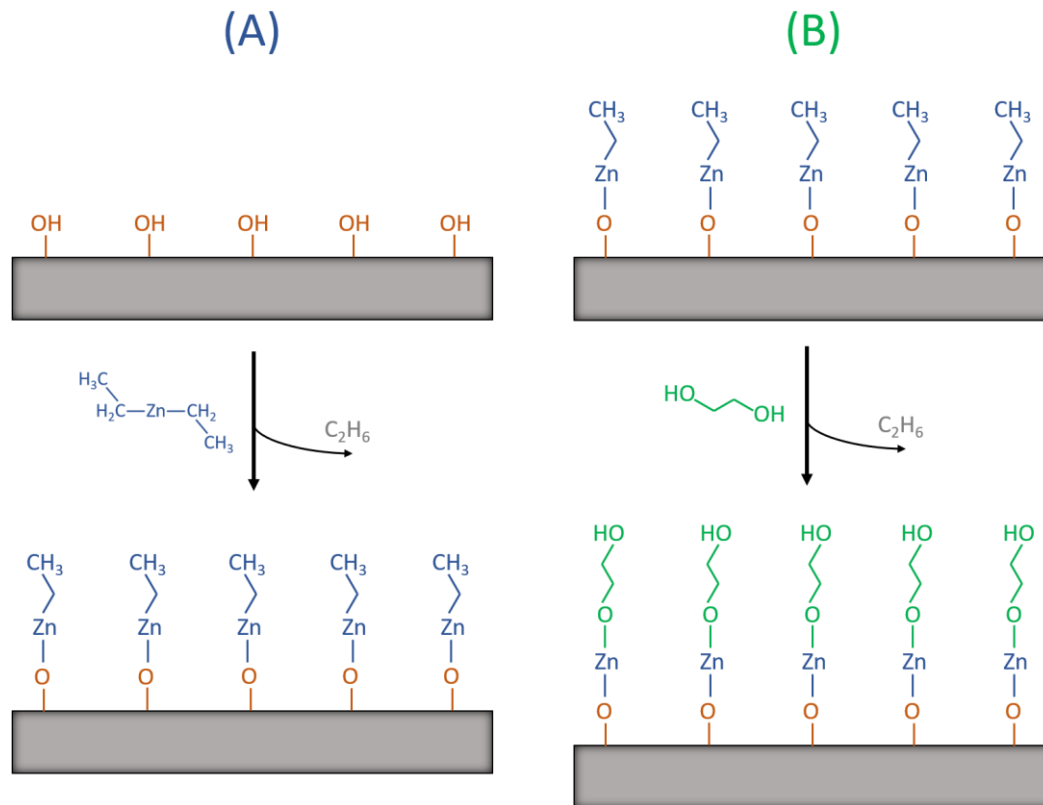


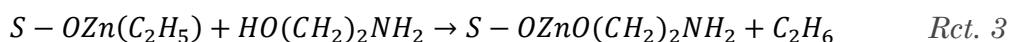
Figure 2: Scheme of two step reaction sequence using (A) Diethylzinc (DEZ) and (B) Ethylene glycol (EG).

In Figure 2 (A) the reaction of the gaseous DEZ (Rct. 1) at the sample surface is shown. The DEZ molecule splits off one ethyl group and binds to the surface hydroxyl group emitting ethane as reaction by-product. This reaction can only take place up to the moment that all hydroxyl groups at the surface are occupied with DEZ molecules. A reaction between DEZ and the ethyl groups of the new surface is not possible and therefore the reaction is self-limiting.

As the surface is now totally covered with one monolayer of the DEZ reaction product the excess DEZ molecules and the byproducts are purged out of the vacuum chamber. Subsequently the second step in the AB sequence (Rct. 2) shown in Figure 2 (B) is started. EG gas is exposed to the surface and one of the hydroxyl groups of the molecules reacts with the ethyl group on the surface. This reaction takes place as long as all surface positions are occupied by the EG molecules. Similar to the first step the residual EG gas and the reaction byproducts are purged out of the chamber leaving behind again a surface covered with hydroxyl groups. By repeating this two steps a film of alternating monolayers can be grown.

In comparison to the AB process the supposed reactions during the ABC deposition and related schemes follow (The absent Reaction (A) is the same as Rct. 1 above and therefore not repeated here):

(B)



(C)

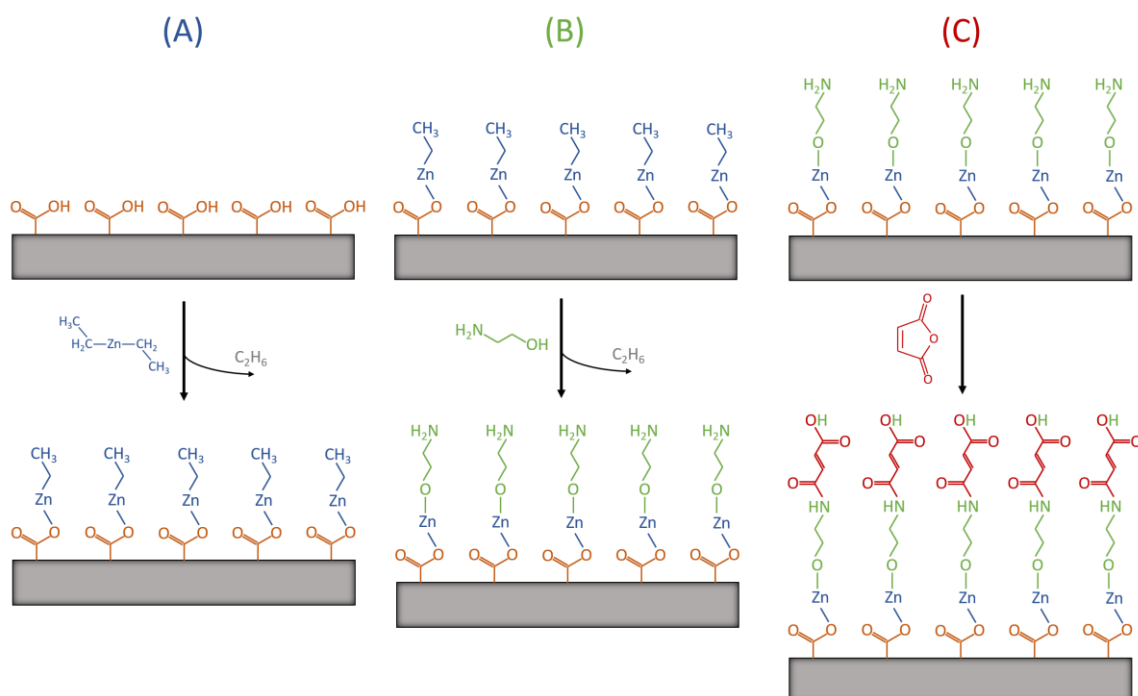
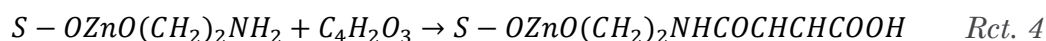


Figure 3: Scheme of three step reaction sequence using (A) diethylzinc (DEZ), (B) ethanolamine (EA) and (C) maleic anhydride (MA).

In Figure 3 (A) DEZ reacts with the carboxylic group to form  $Zn(C_2H_5)_2$  species (Rct. 1) as a first step in the ABC sequence similar to the primary step in the AB process. In step B of Figure 3 the new formed surface species reacts preferentially with the hydroxyl end of EA forming  $ZnO(CH_2)_2NH_2$  and emitting ethane as a byproduct (Rct. 3). Different from the reaction with EG, EA leaves behind a surface covered with amine groups and none of the two molecule functional groups is able to react with it.

The last step of the ABC sequence is shown in Figure 3 (C). MA reacts with the amine group on the surface through a ring-opening reaction forming carboxylic groups at the surface (Ret. 4). When the sequence is repeated a zincone film with three alternating layers can be grown.

To ensure that reactions only take place at the sample surface the precursors are not allowed in the reaction chamber at the same time. Thus, the precursors have to be introduced in very short pulses and between two exposure steps a purging step has to be introduced. An inert purging gas serves as carrier gas for the excess precursor molecules which do not react on the surface as well as for the reaction byproducts and transports them out of the reaction chamber. Therefore for every precursor exposure step an additional purging step has to be defined.

All steps of the MLD sequence until the first repetition form one cycle. For every MLD cycle, a layer of the used precursors is deposited. Therefore, in theory, a linearly growing film is deposited. The so called growth per cycle (GPC) can be defined.

For every MLD process one has to find the optimal recipe. On the one hand all surface groups have to be occupied by the according precursor in the exposure step. On the other hand, according the purging step, no precursors of previous steps can be allowed in the reaction chamber apart from those bonded to the surface. In other words, for all steps the GPC has to be in saturation, as can be seen from the so called saturation curves. In case of the exposure step the saturation curve shows the GPC as a function of the precursor injection time (exposure time). In case of the purging step the saturation curve shows the GPC as function of the purging time. For long enough exposure time or purging time one reaches a plateau in which the change in GPC is neglectable. In Figure 4 theoretical saturation curves are shown.

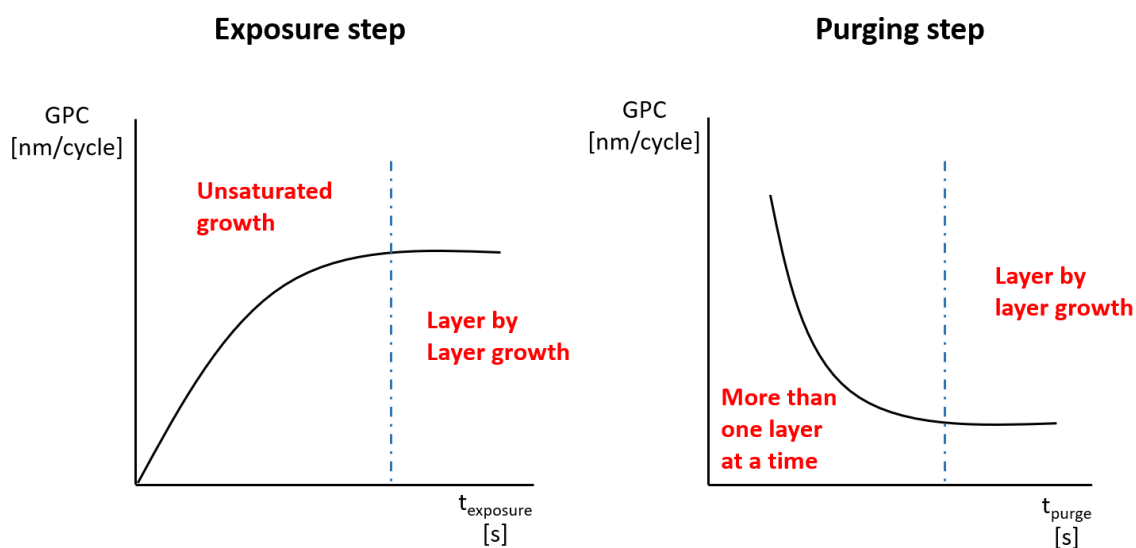


Figure 4: Saturation curves

In general, to obtain the parameters needed for the saturation curves a reasonable number of depositions have to be made for every exposure and purging step. During every deposition either  $t_{\text{exposure}}$  or  $t_{\text{purge}}$  is varied and the GPC is measured. Then, models for the exposure step and the purging step have to be applied to achieve reasonable fitting functions.

### **Precursor exposure step:**

The time  $t_{\text{exposure}}$  is defined as the open time of the valve between the vessel of a precursor and the reaction chamber. During this short time period the precursor gas is able to react on the surface of the sample.

As mentioned above the exposure time has to be long enough to ensure the occupation of every free surface functional group with the according precursor molecules. In the case that the opening time of the valve is too short the growth is unsaturated and therefore a complete monolayer cannot be build.

Increasing the time  $t_{\text{exposure}}$  after reaching saturated growth makes no difference because all surface groups are occupied. Furthermore, a reaction between the precursor and the new surface is not favored.

The derivation of the according fitting function has already been performed in the master thesis of Richard Berger [8]. The final form of the fitting function is plotted below (Equation 1) with consent of the author.

$$GPC_{(t_{\text{exposure}})} = G * (1 - e^{-C_2 * (t_{\text{exposure}} - t_0)}) \quad \text{Equation 1}$$

*GPC<sub>(t<sub>exposure</sub>)</sub>* ... growth per cycle for exposure time *t<sub>exposure</sub>*  
*G* ... GPC in saturation regime  
*C<sub>2</sub>, t<sub>0</sub>* ... fitting parameters

### **Purging step:**

For the purging step the valves of the precursors are closed and the purging gas argon is carrying out the reaction by-products and the residual precursor gas towards the vacuum pump. Therefore, the time  $t_{\text{purge}}$  is the time in which all precursor valves are closed and only argon is injected into the reaction chamber.

If  $t_{\text{purge}}$  is too short precursor molecules of the previous step are still in the chamber and react with the next precursor already in the gasphase. This leads to a growth in which more than just one monolayer is build in one step.

For longer  $t_{\text{purge}}$  more and more precursor molecules are carried out of the reaction chamber until nearly no gas phase reactions can take place in the next precursor step. The according fitting function is shown in Equation 2.

$$GPC_{(t_{\text{purge}})} = G + A * e^{(-C_1 * t_{\text{purge}})} \quad \text{Equation 2}$$

*GPC<sub>(t<sub>purge</sub>)</sub> ... growth per cycle for purge time t<sub>purge</sub>  
G ... film growth due to reactions with surface functional groups  
A, C<sub>1</sub> ... fitting parameters*

### 2.1.2 Zincone Films

There are already papers (listed below) reporting zincone films produced by MLD. Most of the research has been focusing on aluminum based alucones. Although the precursor employed by MLD to add the zinc part has always been DEZ, an increasing number of different organic precursors is utilized.

Brown et al. [9] used Propane-1,2,3-triol or glycerol and DEZ to coat carbon nanotubes with a growth rate of 1.3 Å/cycle at 150°C. They were able to improve the values for Young's modulus.

Diacetylene glycol and DEZ was applied by Cho et al. [10] with an additional step of UV polymerization. A growth rate of 5.2 Å/cycle could be measured at 100–150°C. They produced high performance two dimensional zinc oxide cross-linked polydiacetylene.

With a growth per cycle of 1.6 Å/cycle at 150°C a MLD film of alternating DEZ and Hydroquinone could be deposited by Yoon et al. [11] among others. The film may be a promising candidate for displays and thin film photovoltaic devices.

Sood et al. [12] applied in a two step MLD process DEZ and the heterobifunctional precursor 4-Aminophenol and reported a constant growth rate of 1.1 Å/cycle in the temperature range of 140-200°C.

Further organic precursors that are used together with DEZ are Glycidol, Oxine [13] and EG, which can be found in different reports [6, 7, 14]. Yoon et al. [15] deposited on ZrO<sub>2</sub> at temperatures between 90°C and 170°C. He discovered a strong dependency of growth rate on the deposition temperature, e.g. 4 Å/cycle at 90°C and 0.25 Å/cycle at 170°C. Furthermore, a deposition on a silicon wafer was carried out at 130°C that showed a growth rate of 0.7 Å/cycle. Liang et al [16] coated titania particles with a growth rate of 0.25 Å/cycle at 120°C. Using the same reactor as in this work Perrotta et al. [7] produced Zincone films at 110°C with a growth rate of 1.05 Å/cycle.

Those samples above show how large the margin in growth rate is and reflect the opportunities of MLD. Different growths per cycle can be achieved either by using different precursor materials but also the setup and the process temperature show large significance.

In this work, the step to an ABC deposition is made using DEZ, EA and MA. A paper could be found using trimethylaluminum (TMA) as metallic precursor and EA and MA as organic ones [5] but the zincone delivery with these precursors seems to be a completely new attempt.

### 2.1.2.1 Zincone via DEZ and EG

The schematic structure of the zincone film deposited with DEZ and EG can be seen in Figure 5:

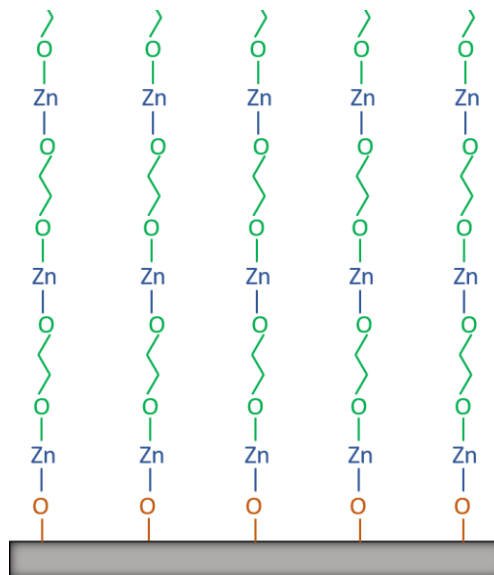


Figure 5: Zincone film deposited with DEZ and EG

Figure 5 suggests that the film thickness deposited in one MLD cycle should be in the region of the length of the two bonded precursor molecules. In the ideal case every surface group is standing perpendicular to the substrate and all of them bind a precursor molecule. The precursor molecules are not allowed to react with themselves and thereby single chains of the reactants grow perpendicular out of the surface.

Measurements of the film thickness though show that the GPC is much lower than this theoretical approach shows. There are different possible reasons for the minor growth. One is that the precursor chains growing out of the surface are not perpendicular but tilted, what seems to be especially for longer organic molecules the case. Another reason that is attributed to the homobifunctionality of the organic precursor molecule is a possible double-reaction with the surface. This would lead to a reduction of active surface sites and therefore hinder the growth [13]. A third mechanism that can take place is the reaction with water. In this case a water molecule reacts with the ethyl group of DEZ at the surface, passivating it for a reaction with EG. The different mechanism for the reduction of the GPC are shown in Figure 6.



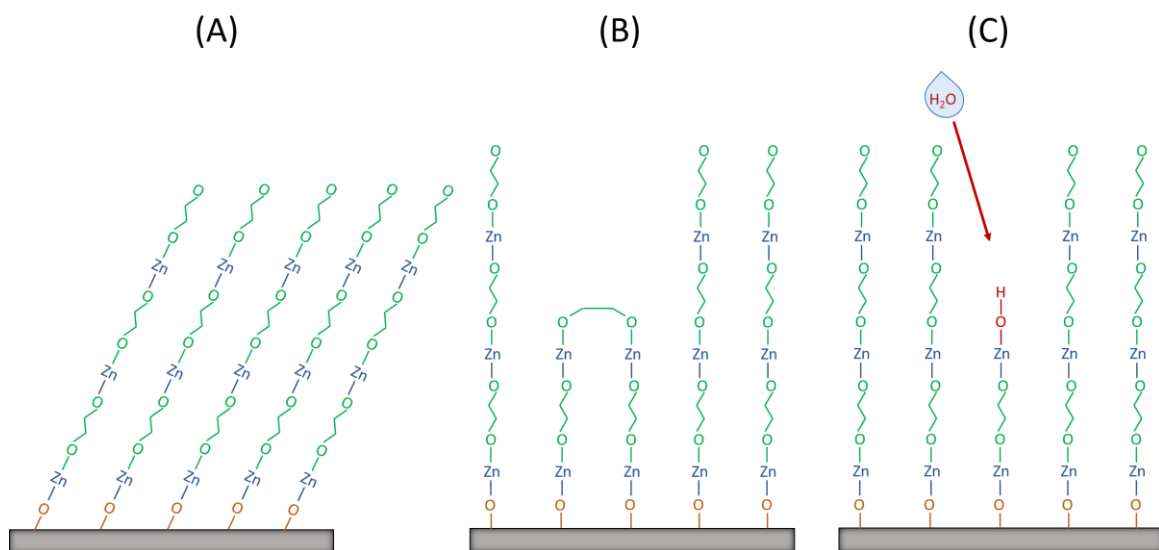


Figure 6: (A) tilted molecules, (B) double reaction, (C) passivation reaction with water

### 2.1.2.2 Zincone via DEZ, EA and MA

The schematic structure of an ABC MLD cycle utilizing DEZ, EA and MA is shown in Figure 7:

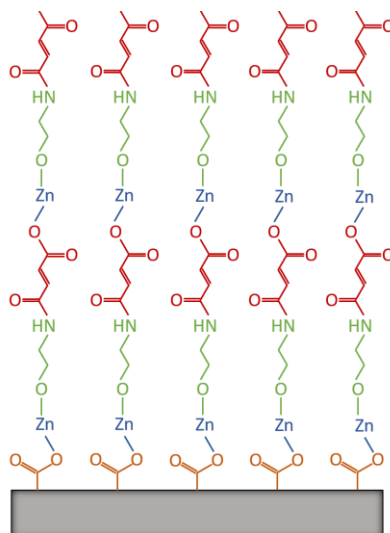


Figure 7: Zincone film deposited with DEZ, EA and MA

Similar to the AB deposited film the GPC is lower than the length of the precursor molecules. Tilted chains and reactions with water are likely mechanisms that cause hindered growth. Although double-reactions can be avoided due to the application of an hetero-bifunctional and an ring-opening reactant, the forming of a maleimide ring could occur [13]. A schematic picture of the different mechanisms is shown in Figure 8.

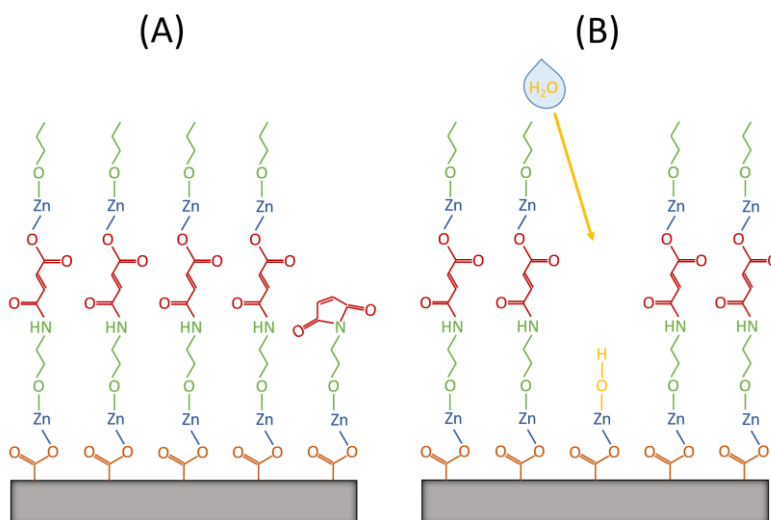


Figure 8: (A) forming of maleimide ring, (B) passivating reaction with water

### 2.1.3 Porous Crystalline ZnO from Zincones Films

The weakly bonded organic parts of the zincones can be removed in different ways. The easiest one is by heating up the sample in the presence of oxygen and therefore “burning” away the organic part resulting in a zinc and oxygen containing structure with vacancies in between. Due to the different lengths of the organic chains in the AB and ABC film the size of these pores should be different. A scheme of this procedure can be seen in Figure 9.

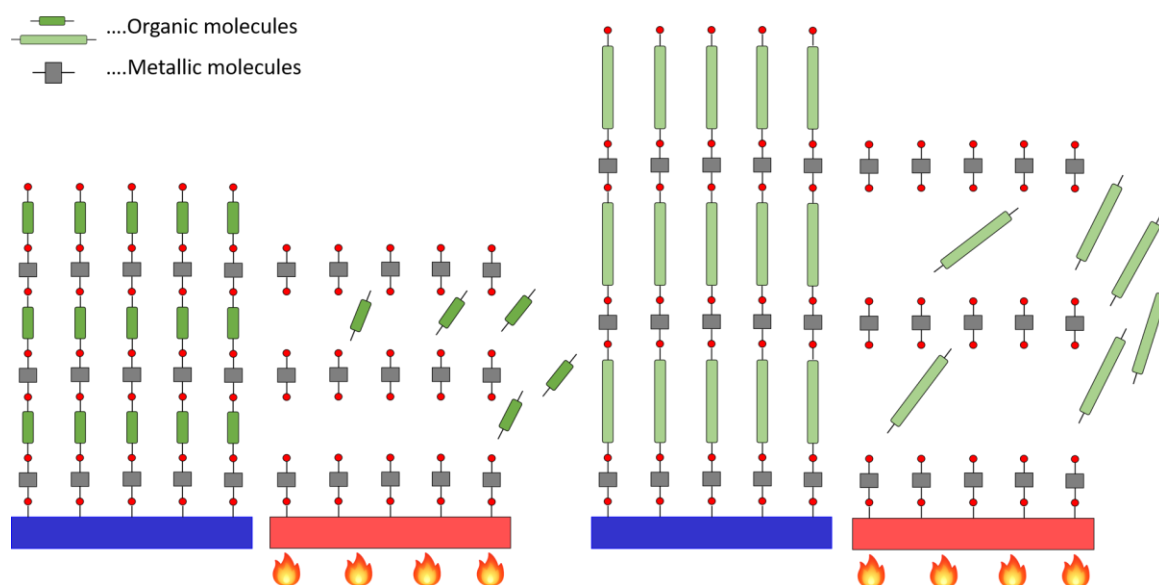


Figure 9: Scheme of the production of porous ZnO with different organic molecules

By further heating up the sample a rearrangement of the zinc and oxygen atoms can be observed leading to a crystalline and porous zinc oxide structure.

Other possibilities to remove the organic parts are water etching or the treatment with plasma, which was also investigated in this thesis. In the case of treatment with plasma reactive species are created by plasma and directed to the sample surface where they react with the organic parts. Typical gases for the plasma creation are  $O_2$ ,  $N_2$  or  $H_2$ .

## 2.1.4 Photocatalytic Test

Zinc oxide and titanium dioxide are materials which have been successfully applied as photocatalysts and used in many cases like self-cleaning window or wastewater treatment. [17]

There are different ways to increase the photocatalytic activity of ZnO such as doping with Cu Atoms [18] or increasing the surface area [19].

A popular method to proof the photocatalytic activity of a sample is the degradation of a methylene blue (MB) dye under UV-light. All that is required for the test is the measurement of the rate of photocatalytic bleaching of MB in aqueous solution via UV/vis spectrophotometry. A scheme of this method is shown in Figure 10.

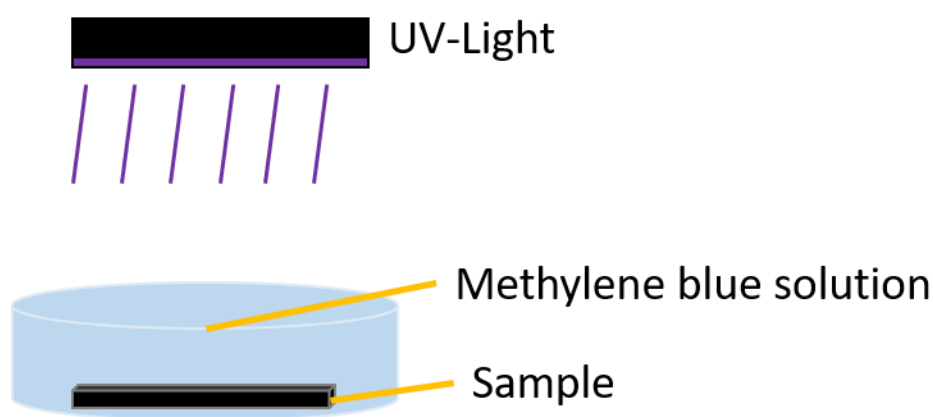
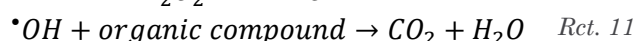
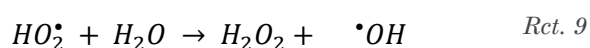
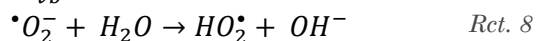
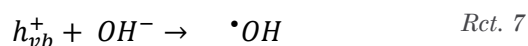
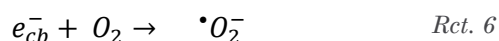
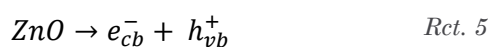


Figure 10: Scheme of photocatalytic test

The mechanism for the decolorization of the dye is believed to be as follows [18]:



Photons with equal or higher energy than the band gap of ZnO are absorbed. Thus, electrons are promoted from the valence band to the conduction band ( $e_{cb}^-$ ) leaving a hole in the valence band ( $h_{vb}^+$ ). This leads to the formation of hydroxyl radicals which react with the organic compound.

## 2.2 CHARACTERIZATION METHODS

### 2.2.1 Fourier Transform Infrared Spectroscopy (FTIR)

FTIR spectroscopy is a commonly used method to determine the chemical composition of a material. The information is gained by analyzing the interaction of a sample and infrared radiation. When the infrared (IR) light is passing through a sample different vibrations of covalent bonds can be triggered by absorbing the energy of the beam. By measuring this absorption spectrum one obtains unique textures for specific bonds and therefore information of the chemical composition of the examined material.

By introducing the Michelson interferometer one can apply a broad band IR light source rather than using monochromatic radiation. Therefore the absorption spectrum of all containing wavelengths can be obtained. Compared to scanning spectrometer the advantages of the Michelson interferometer are a shorter scan time for a given resolution because of the simultaneous collection of information from all wavelengths. Further more more light is able to interact with the sample because of the omission of entrance and exit slits. This results in a higher signal to noise ratio and a more accurate wavelength enhancing the resolution. A scheme of the Michelson interferometer is shown in Figure 11.

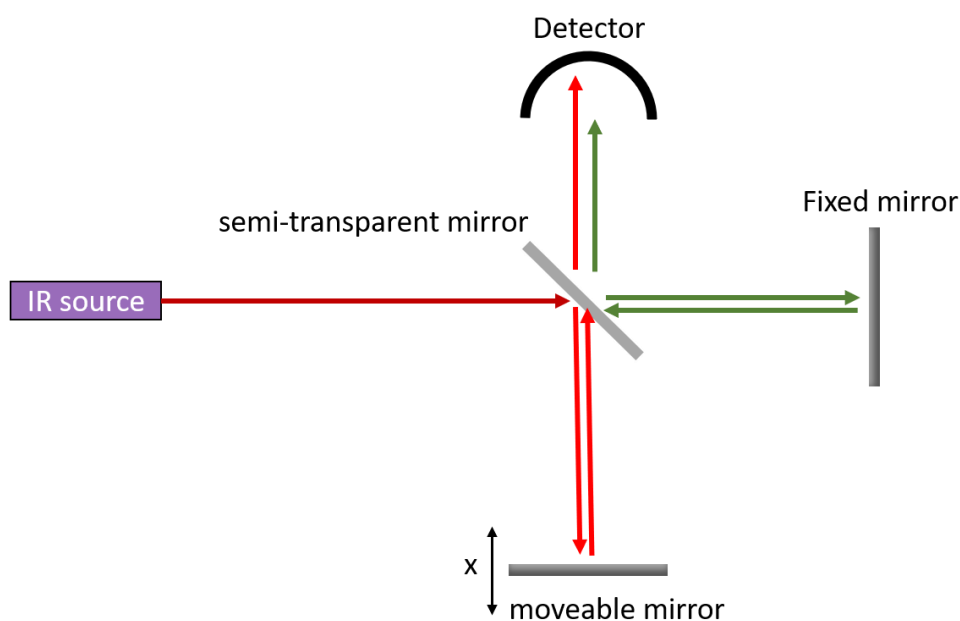


Figure 11: Schematic setup of Michelson interferometer

In principle the Michelson interferometer consists of a source that emits a broad infrared spectra, one semitransparent mirror, two nontransparent mirrors and the detector. The beam is directed to the semi-transparent mirror or beam splitter which, as the name suggests, splits the beam. One part of the wave is traveling to a fixed mirror and the other part is lead to a moveable mirror. Both beams get reflected and recombine at the beam splitter where they are guided to the detector. By moving one of the mirrors while the other one is fixed constructive and destructive interference occurs. The detector measures the intensity of the beam for the whole IR spectrum as a function of the displacement of the moving mirror, the so called interferogram. By applying a Fourier transformation a intensity vs frequency spectrum is obtained which represents the spectral composition of the measuered light. When the recombined beam penetrates a sample the absorption spectrum of this sample can be calculated by removing the spectra without a sample from the one with the sample in the pathway of the beam.

## 2.2.2 X-Ray Diffraction (XRD)

X-Ray Diffraction is a method to obtain information about the crystallographic structure of a material. Monochromatic X-ray photons are elastically scattered by atoms in different planes of a periodic lattice. The X-rays that are diffracted at different planes have different path lengths to travel and either constructively or destructively interfere with each other (Figure 12). Constructive interference occurs when the Bragg-equation (Equation 3) is fulfilled. This means that constructive interference only occurs when the path difference ( $2d\sin\theta$ ) is a multiple of the wavelength of the X-rays. As the wavelength is known and the angles at which constructive interference occurs are measured, the distance between two lattice planes can be calculated. The schematic representation of the bragg equation is shown in Figure 12.

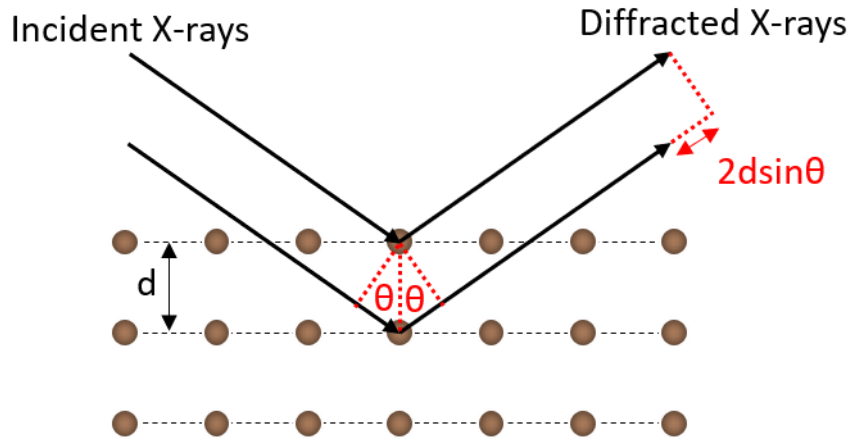


Figure 12: Schematic representation of bragg equation

$$n\lambda = 2d\sin\theta$$

Equation 3

*n ... integer number*  
*λ ... wavelength of X-ray beam*  
*d ... distance between latticeplanes*  
*θ ... Bragg angle*

A more detailed look into XRD can be found in [20].

### 2.2.3 Spectroscopic Ellipsometry (SE)

Spectroscopic Ellipsometry (SE) is an optical technique that can be used to determine the index of refraction and the thickness of thin films. In SE a linearly polarized light is reflected at a non normal angle on the sample. The polarization state of the light is changed upon reflection and the amplitude ratio  $\Psi$  and phase shift  $\Delta$  is measured by a detector. The linearly polarized light can be resolved into a combination of a s-polarized part where the electric field is normal to the plane of incidence and a p-polarized part where the electric field is parallel or in the plane of incidence. The Fresnel equations can be applied to derive amplitude ratio and phase shift upon reflection at a single interface (Equation 4 & Equation 5).

$$r_p = \frac{E_{rp}}{E_{ip}} = \frac{n_1 \cos(\theta_0) - n_0 \cos(\theta_1)}{n_1 \cos(\theta_0) + n_0 \cos(\theta_1)} \quad \text{Equation 4}$$

$$r_s = \frac{E_{rs}}{E_{is}} = \frac{n_0 \cos(\theta_0) - n_1 \cos(\theta_1)}{n_0 \cos(\theta_0) + n_1 \cos(\theta_1)} \quad \text{Equation 5}$$

$$\tan\Psi e^{-i\Delta} = \frac{r_p}{r_s} \quad \text{Equation 6}$$

- $r_p$  and  $r_s$ ... reflection coefficient of p- and s- component of the light
- $E_{rp}$  and  $E_{ip}$  ... complex amplitudes of parallel electric field for incident and reflected light
- $E_{rs}$  and  $E_{is}$  ... complex amplitudes of perpendicular electric field for incident and reflected light
- $n_1$  and  $n_0$  ... refractive indices of the two different media
- $\theta_0$  ... angle of incident light to the normal of the interface
- $\theta_1$  ... angle of transmitted light to the normal of the interface

For reflections at multilayer interfaces the measured  $\Psi$  and  $\Delta$  cannot directly be converted into the wanted parameters of the sample. Therefore a model wich considers the refractive index and thickness of all different layers has to be utilized. The Fresnel equations are applied to calculate  $\Psi$  and  $\Delta$  of the model that matches best the experimental data.



For transparent materials the Cauchy model is a frequently used tool to set the refractive index in relation to the wavelength (Equation 7).

$$n = A + \frac{B}{\lambda^2} + \frac{C}{\lambda^4}$$

*Equation 7*

*n ... refractive index  
λ ... wavelength  
A, B, C ... fitting parameters*

## 2.2.4 Ellipsometric Porosimetry (EP)

Ellipsometric porosimetry (EP) is a method to obtain the open porosity of a sample. In principle EP exploits the change of the refractive index when a probing vapour is adsorbed inside the pores. By continuously increasing the amount of the probing vapour (for instance water steam in the air) and simultaneously measuring the refractive index the amount of adsorbed vapour can be calculated. The effective medium approximation (EMA) is the tool to estimate the volume fraction of the liquid inside the sample. When the partial pressure of the vapour reaches the saturation vapour pressure of the atmosphere all accessible pores are filled and the volume fraction calculated with EMA is identical to the fraction of open pores. The scheme of the porosimetry measurement is shown in Figure 13.

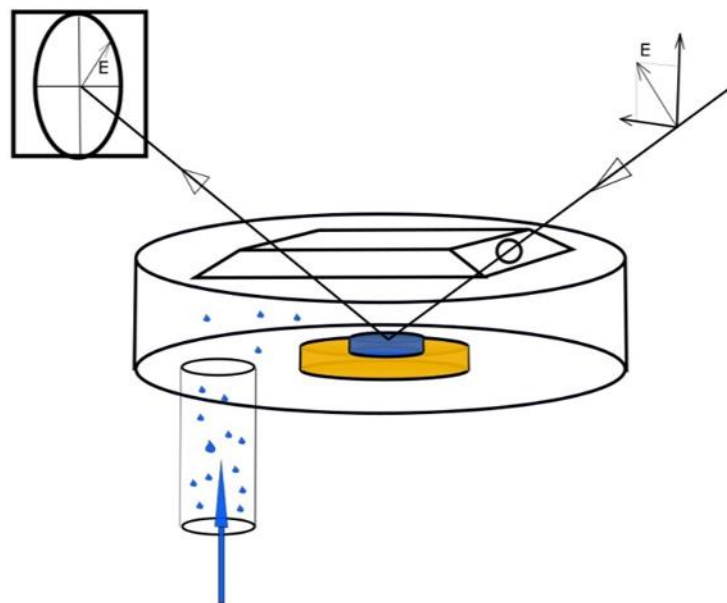


Figure 13: Ellipsometric porosimetry measurement principle, (scheme reprinted with consent of author [8])

As well as the fraction of open pores a pore size distribution can be calculated by using the obtained information of the measurement and applying the Kelvin equation. More information about EMA and the calculation of the pore size distribution can be obtained in the according chapters below.

### 2.2.4.1 Effective Medium Approximation (EMA)

By applying the effective medium approximation the volume fraction of an adsorbed probing vapour inside a porous film can be calculated. Therefore, the refractive index of the probing material has to be known and the refractive index of the compound has to be measured.

Starting with the Lorentz-Lorenz effective-medium expression for the effective dielectric function of a two compound material a formula can be derived that is only dependent on the refractive index of the sample in air and probing vapour atmosphere and the refraction index of the condensed vapour. The derivation of the formula and more information can be found in [8].

$$\frac{V_{probe}}{V} = \frac{\frac{n^2 - 1}{n^2 + 2} - \frac{n_0^2 - 1}{n_0^2 + 2}}{\frac{n_{probe}^2 - 1}{n_{probe}^2 + 2}} \quad \text{Equation 8}$$

$V_{probe}$  ... Volume of condensed probing vapour in film  
 $V$  ... total volume of film  
 $n$  ... measured refractive index of film containing probing condensat  
 $n_0$  ... measured refractive index of film in air  
 $n_{probe}$  ... refractive index of the condensed probing gas

### 2.2.4.2 Pore size distribution

Starting from the Kelvin equation [21] a distribution of the pore sizes inside a mesoporous film can be calculated. Therefore, the mean radius of curvature of a liquid, the so called Kelvin radius, is brought in relation with the relative pressure.

$$\frac{2}{r_k} = \frac{1}{r_1} + \frac{1}{r_2} = -\frac{RT}{\gamma V_L \cos(\theta)} \ln\left(\frac{p}{p_0}\right) \quad \text{Equation 9}$$

$r_k$  ... Kelvin radius  
 $r_1, r_2$  ... radii of meniscus curvature  
 $\gamma$  ... surface tension  
 $V_L$  ... molar volume  
 $\theta$  ... contact angle  
 $R$  ... gas constant  
 $T$  ... Temperature  
 $p/p_0$  ... relative pressure

As the meniscus formation depends on the geometry of the pores an assumption for the shape of the pore has to be made. Typically for the calculation a cylindrical shaped pore is assumed which in most cases is sufficiently accurate and avoids too complicated models. For the adsorption this simplifies the equation because  $r_2$  becomes infinite and  $r_1$  is the pore radius. Another simplification that can be made is only considering the adsorption part because the contact angle can be neglected. Therefore, a term for the maximum radius of the filled pores can be written as:

$$r_{pore} = \frac{\gamma V_L}{RT \ln\left(\frac{p_0}{p}\right)} \quad \text{Equation 10}$$

With EMA and Equation 10 the cumulated fraction of condensed probing vapour inside a pore and the corresponding maximum radius can be brought in relation. Finally the PSD is achieved by taking the derivative of the cumulation function with respect to  $r_{pore}$  against  $r_{pore}$ .

$$dV_{ads}(r_{pore}) = \frac{\partial V_{ads}(r_{pore})}{\partial r_{pore}} * dr_{pore} \quad \text{Equation 11}$$

$V_{ads}(r_{pore})$  ... cumulative volume of water adsorbed in pores with a radius  $r < r_{pore}$

### 3 THE MLD SYSTEM

---

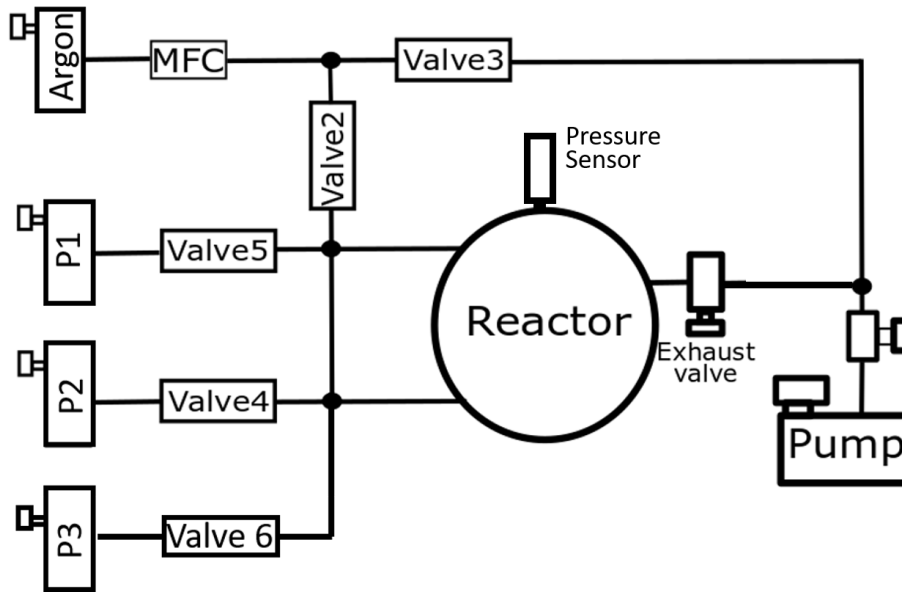


Figure 14: Scheme of the MLD system

Figure 14 shows the scheme of the MLD system that was utilized to produce the desired thin films. The original system was built by Richard Berger in the course of a previous thesis [8]. The system consists of a reaction chamber (Reactor) that is connected to a rotary vane vacuum pump (Dev 1) on the one side and to vessels (P1, P2 and P3) of the precursors at the other side. The purging gas argon is connected to the system via two lines. One line is only a bypass line and is led to the pump, the other line is connected to the precursor lines where it can be mixed with the reactant during operation. The amount of purging gas is controlled by the massflow controller (MFC, Dev 8). Both argon lines and the three precursor lines can be separated from the system by valves, whereby the ones of the precursors are special ALD valves (valve 4,5 and 6, Dev 6) and the other two (valve 2 and 3, Dev 7) are simple mechanical valves. A microcontroller (Dev 9) is used to control the position of the different valves. The pressure inside the reaction chamber is measured with a pressure sensor (Dev 11) and the pump can be disconnected by a manual valve (Exhaust valve).

To be able to deposit a film with three different precursors instead of only two, the line to valve 6 and vessel P3 was attached to the original system. Reproducibility is not always easy to achieve because of many factors impacting the outcome of the deposition. Hence, a few controllable parameters should be fixed to at least reach comparable results. Despite of the precursor injection times and the purging times which have to be controlled in a very accurate way the temperature control and proper insulation is a very important factor. The next chapters show the importance of those requirements.

### 3.1 REACTOR AND LINE HEATING

In order to control the process temperature and temperature of the precursor reactants heating wires (Dev 2) and a heating disk (Dev 3) are employed together with the temperature controllers (Dev 3 & Dev 4). Depending on the vapour pressure of the precursor the vessels have to be heated to different temperatures. Therefore, separated heating circuits are applied. A major challenge for the MLD process is the condensation of precursor molecules inside the reactor or in one of the lines. This would lead to a constant outgassing of the formed condensate that could not be purged away. A perfect layer by layer growth would be impossible to achieve because of the presence of different gaseous reactants at the same time. This has to be prevented as well as possible. Therefore a temperature gradient from the precursor vessel to the reactor was implemented by utilizing small heating circuits. All heated parts were isolated with aluminum foil and pipe isolation.

The scheme of the circuit arrangement (left) and a picture of the isolated reactor (right) can be seen in Figure 15.

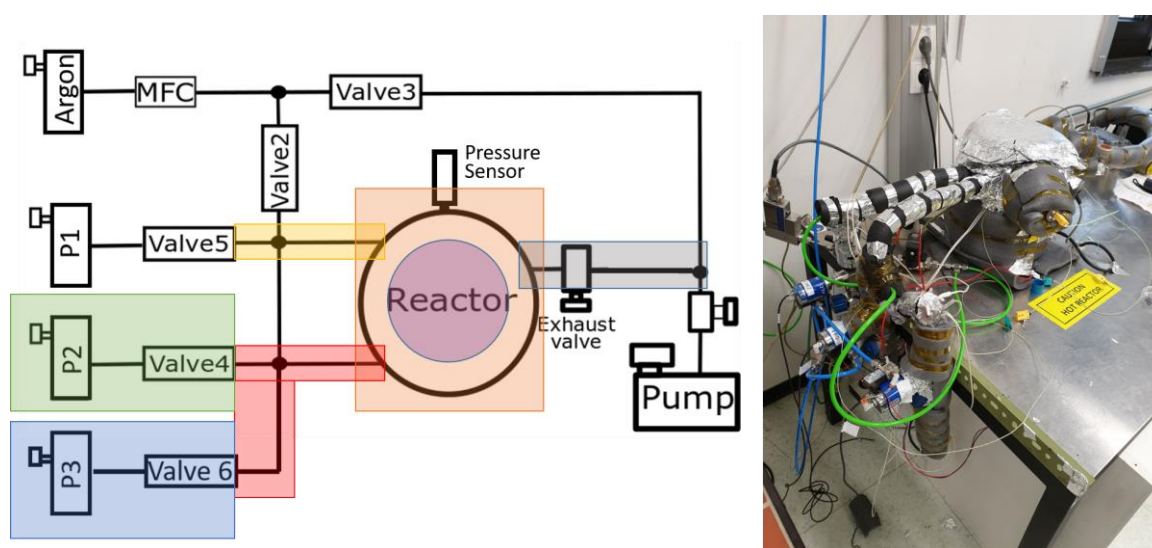


Figure 15: Left: Scheme of heating circuits (rectangle are heating wires, circle is heating disk) and right: picture of isolated system.

Different precursors were used for the AB- and ABC-deposition resulting in different temperatures of the parts. An overview of the temperatures of the different parts can be seen in Table 1.

	Heating circuit	Temperature [°C]
AB-deposition	Reactor wire	110
	Reactor disk	107
	DEZ line	60
	EG line	95
	EG vessel	80
	Exhaust line	80
ABC-deposition	Reactor wire	60
	Reactor disk	60
	DEZ line	42
	EA and MA line	55
	EA vessel	50
	MA vessel	50
	Exhaust line	60

Table 1: Temperatures of the different parts for AB- and ABC- deposition (colors correspond to Figure 15)

The temperatures of the AB-deposition were held the same as in the work of Richard Berger [8] since the results should be reproduced.

### 3.2 MASS FLOW CONTROLLER, REACTOR VOLUME, LEAK RATE

As can be seen in Figure 14 in the previous chapter the flow of the purging gas argon is controlled by a mass flow controller (MFC). The flow rate can be set in an according software (in-house programmed) on the computer, which is connected to the MFC over a communication module. The Argon is not only used to purge out the residual reactants and by-products of the previous deposition step but also serves as a carrier gas for the precursor molecules. Therefore a constant Argon flow is maintained during the whole process.

The reactor volume is essential for the calculation of the leak rate and therefore has to be determined beforehand. This is achieved by firstly evacuating the system and then closing the valve to the pump. Subsequently, a known constant gas flow is set and the pressure increase in the chamber is measured. The calculation of the volume is then achieved by applying Equation 12 [22].

$$V = \frac{q\Delta t}{\Delta p} \quad \text{Equation 12}$$

*V ... Volume of reactor*  
*q ... gas flowrate*  
 *$\Delta p$  and  $\Delta t$  ... pressure increase in according time interval*

The volume of the reactor for the AB-deposition was calculated to be  $V = 5$  l. The third line that was added for the ABC-deposition has a neglectable small volume. Therefore the same reactor volume of  $V=5$  l was used for further calculations.

To ensure a proper deposition and prevent water from being involved in the reactions unintentionally the system has to be tested for leaks. As leaks can originate in many different ways (e.g. porous gasket, small holes in plastic tubes) and at all times the leak rate has to be measured before every deposition. The leakrate is defined as the pressure increase per time in a known volume. This is measured by separating the pump from the evacuated reactor and measuring the pressure increase due to a particle flow through the leaks into the reactor (Equation 13).

$$Q_L = \frac{\Delta p}{\Delta t} V \quad \text{Equation 13}$$

*$Q_L$  ... Leak rate*  
*V ... Volume of reactor*  
 *$\Delta p$  and  $\Delta t$  ... pressure increase in according time interval*



For the calculation of the reactor volume and the leakrate matlab programs [8] were used. For the volume calculation the gas flowrate and the according pressure increase in a time interval from the pressure sensor is needed. The program for the leakrate requires the volume of the reactor and the pressure increase, whereby a linear regime has to be defined.

## 4 EXPERIMENTS & RESULTS

---

### 4.1 THE DEPOSITIONS

For all depositions, whether AB- or ABC-deposition, single side polished Si-wafers with an average native oxide thickness of 0.9 nm were used as substrate. Therefore the wafers were cut into square-shaped samples of around 1-2 cm<sup>2</sup>. Depending on the deposition between 4 and maximum 14 of such samples could be placed into the reaction chamber. Another process parameter that was applicable for both process types was the Ar-flow rate that was set to *16 sccm* for all depositions. Theoretically this would fix the process pressure  $p_{Ar}$  to a constant value. Due to wear parts of the pump a certain variability in the process pressure was observed. Even though the oil was changed frequently since then the suction power of the pump decreased. Therefore the process pressures of the AB- and ABC-depositions are different.

After the executed deposition the samples were removed from the vacuum chamber and directly measured in the ellipsometer to obtain the thickness and index of refraction.

### 4.1.1 AB-depositions

The AB-deposition refers to the deposition in which DEZ and EG are used as precursors. A recipe of the necessary process steps that are composed of manual steps as well as steps that are controlled by the microcontroller can be seen in Table 2 (Valve numbers correspond to Figure 14). The initial setting of the reactor is with samples loaded on the reactor stage, a closed lid and the connection to the rotary vane pump is still shut.

Process step	System setting
1. Initial settings	<ul style="list-style-type: none"> <li>• ALD-valves 4 &amp; 5, mechanical valves 2 &amp; 3 and exhaust valve closed</li> <li>• MFC set to 0</li> </ul>
2. Leak rate estimation	<ul style="list-style-type: none"> <li>• Open exhaust valve</li> <li>• After some adjustment time test leak rate until <math>q_L &lt; 0.1 \text{ sccm}</math></li> </ul>
3. Set Argon flow	<ul style="list-style-type: none"> <li>• Open valve 3</li> <li>• Set MFC to 16 sccm, wait 60 sec</li> <li>• Open valve 2, close valve 3, wait 60 sec</li> </ul>
4.1. DEZ exposure step	<ul style="list-style-type: none"> <li>• Open valve 5, wait <math>t_{\text{DEZ,exposure}}</math> s, close valve 5</li> </ul>
4.2. DEZ purging step	<ul style="list-style-type: none"> <li>• Wait <math>t_{\text{DEZ,purge}}</math> s,</li> </ul>
4.3. EG exposure step	<ul style="list-style-type: none"> <li>• Open valve 4, wait <math>t_{\text{EG,exposure}}</math> s, close valve 4</li> </ul>
4.4. EG purging step	<ul style="list-style-type: none"> <li>• Wait <math>t_{\text{EG,purge}}</math> s</li> </ul>
5. Finalization step	<ul style="list-style-type: none"> <li>• After <math>t_{\text{deposition}}</math> open valve 3, close valve 2, set MFC to 0 sccm, close valve 3</li> </ul>

Table 2: Process steps for AB-deposition

The steps 4.1 to 4.4 are defined as one cycle and repeated depending on the required film thickness. To obtain a proper deposition recipe the parameters  $t_{\text{DEZ,exposure}}$ ,  $t_{\text{DEZ,purge}}$ ,  $t_{\text{EG,exposure}}$ ,  $t_{\text{EG,purge}}$ , have to be optimized and therefore the saturation curves have to be measured (see chapter introduction). As perfect parameters for the AB-deposition with DEZ and EG were already measured for the same setup and no work was done on the reactor in the meantime, the saturation curves were adopted from the previous work [8]. A cutout of the saturation curves can be seen in Figure 16. The process pressure with a constant Argon flow of 16 sccm was around  $2.4 - 2.6 \cdot 10^{-1} \text{ torr}$ .

## Saturation Curves

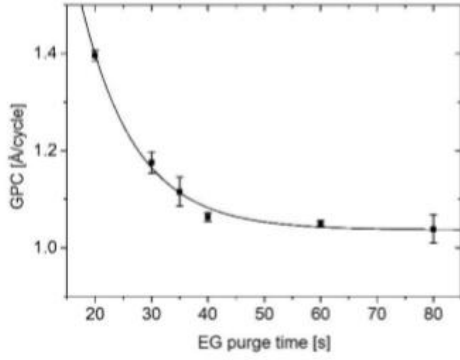


Figure 34: EG purge saturation curve

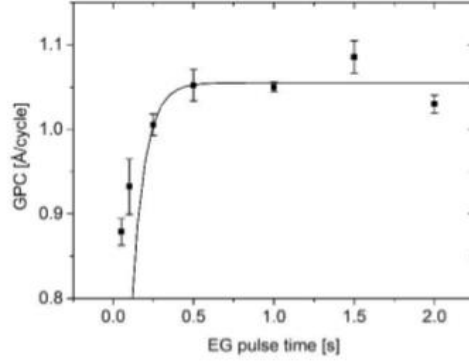


Figure 33: EG pulse saturation curve

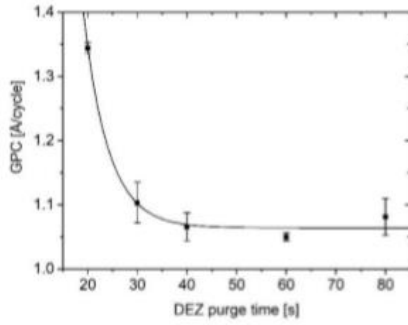


Figure 35: DEZ purge saturation curve

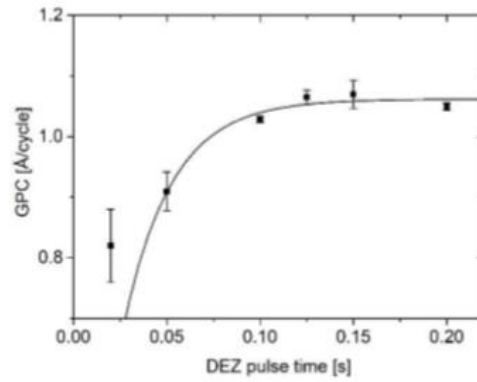


Figure 36: DEZ pulse saturation curve

Figure 16: Cutout of saturation curves (reprinted with consent of author [8])

The optimized parameters can be read out of the saturation curves and result in:

Table 3: Optimized parameters of AB-deposition

$t_{DEZ,exposure}$	$t_{DEZ,purge}$	$t_{EG,exposure}$	$t_{EG,purge}$
0.15 s	60 s	1 s	60 s

The GPC in saturation according to the fitting functions for the saturation curves is:

$$GPC = 1.055 \frac{\text{\AA}}{\text{cycle}}$$

Using the optimized parameters from the table above (Table 3) some samples were produced to make sure that the reactor conditions did not change in the meantime when it was not used. As the GPC in average was very close to the one from the saturation curves the system seemed to be still in the same shape as it was in the previous work [8].

For the SE measurement the ellipsometer (Dev. 14) was used with its original stage. On the connected computer the software completeEASE was applied to configurate the measurement and later also for fitting. To obtain higher precision the samples are measured from four different angles between 60° and 75°. For the fitting model every layer of the sample has to be taken into account. Silicon as the substrate material, the native oxide layer of it and the deposited film. Therefore in the library of the completeEASE software all different kind of models can be found. A model for the Si substrate layer is the SI\_JAW and the corresponding oxide layer is taken into account by the NTVE\_JAW model where the thickness of this layer is a changeable parameter. For the deposited film a Cauchy model (Equation 7) is applied where A and B were used as fitting parameters and C is set to 0. The thickness was used as fitting parameter too and the absorption coefficient was set to 0. The band edge was set to 400 nm because the studied film is transparent for higher wavelengths.

A sample of how the measurement data and the corresponding fit looks like can be seen in the following Figure 17:

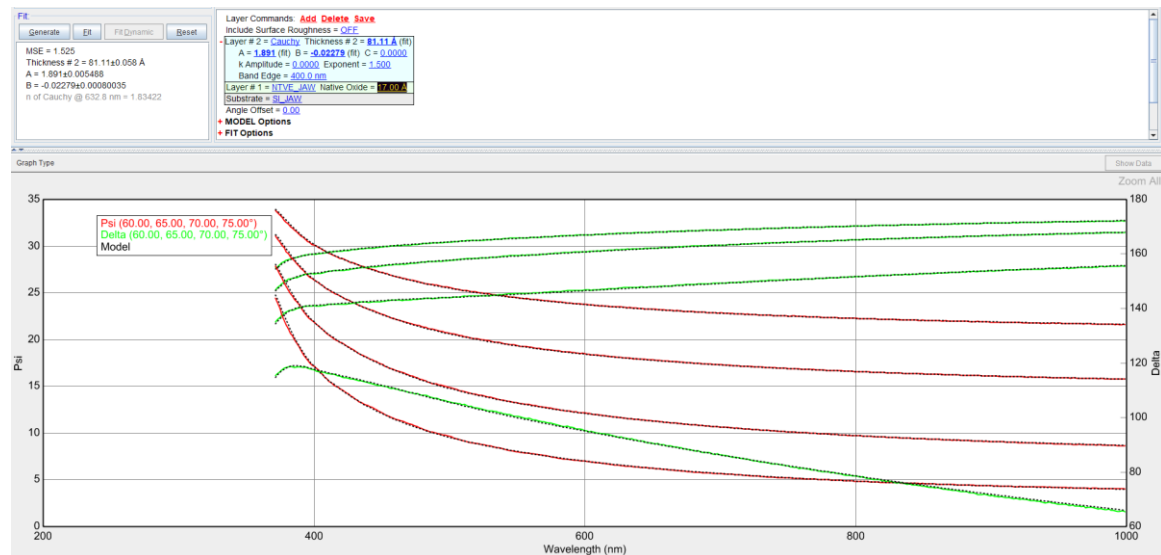


Figure 17: Sample of Ellipsometry measurement

In the measured thickness regimes this model fits quite well.

### 4.1.2 ABC-depositions

DEZ, EA and MA are the precursors used for the ABC deposition. The according process steps can be seen in Table 4.

Process step	System setting
1. Initial settings	<ul style="list-style-type: none"> <li>ALD-valves 4, 5 &amp; 6, mechanical valves 2 &amp; 3 and exhaust valve closed</li> <li>MFC set to 0</li> </ul>
2. Leak rate estimation	<ul style="list-style-type: none"> <li>Open exhaust valve</li> <li>After some adjustment time test leak rate until <math>q_L &lt; 0.1 \text{ sccm}</math></li> </ul>
3. Set Argon flow	<ul style="list-style-type: none"> <li>Open valve 3</li> <li>Set MFC to 16 sccm, wait 60 sec</li> <li>Open valve 2, close valve 3, wait 60 sec</li> </ul>
4.1. DEZ exposure step	<ul style="list-style-type: none"> <li>Open valve 5, wait <math>t_{\text{DEZ,exposure}}</math> s, close valve 5</li> </ul>
4.2. DEZ purging step	<ul style="list-style-type: none"> <li>Wait <math>t_{\text{DEZ,purge}}</math> s,</li> </ul>
4.3. EA exposure step	<ul style="list-style-type: none"> <li>Open valve 4, wait <math>t_{\text{EA,pulse}}</math> s, close valve 4</li> <li>Wait <math>t_{\text{separate}}</math> s</li> <li>Repeat this step <math>n_{\text{EA}}</math> times</li> </ul>
4.4. EA purging step	<ul style="list-style-type: none"> <li>Wait <math>t_{\text{EA,purge}}</math> s</li> </ul>
4.5. MA exposure step	<ul style="list-style-type: none"> <li>Open valve 6, wait <math>t_{\text{MA,pulse}}</math> s, close valve 6</li> <li>Wait <math>t_{\text{separate}}</math> s</li> <li>Repeat this step <math>n_{\text{MA}}</math> times</li> </ul>
4.6. MA purging step	<ul style="list-style-type: none"> <li>Wait <math>t_{\text{MA,purge}}</math> s</li> </ul>
5. Finalization step	<ul style="list-style-type: none"> <li>After <math>t_{\text{deposition}}</math> open valve 3, close valve 2, set MFC to 0 sccm, close valve 3</li> </ul>

Table 4: Process steps for ABC deposition

In the case of ABC deposition the steps 4.1 to 4.6 define one ABC cycle. To obtain the deposition parameters for a perfect layer by layer growth the saturation curves were measured. The ABC films were produced at a process pressure of around  $0.5 \text{ torr}$  with a constant Argon flow of  $16 \text{ sccm}$ .

For the saturation curves one has to pick one of the steps 4.1 to 4.6 to vary the parameters of this step while keeping all other step parameters fixed at such a niveau that it can be assumed that they are in saturation. In case of the DEZ exposure step the parameter  $t_{\text{DEZ, exposure}}$  reflects the time the ALD valve of the DEZ reactant is opened. To achieve a more precise control over the dosing of EA and MA precursors  $t_{\text{EA,pulse}}$  and  $t_{\text{MA,pulse}}$  were kept constant at 1.5 s and 0.1 s respectively and the number of pulses  $n_{\text{EA}}$  and  $n_{\text{MA}}$  was varied. This approach was chosen because for this reactants the pressure inside the vessels decreased below the desired vapour pressure when the valve was opened for too long.

As the purging times are much longer than the exposure times it is time-saving to start with the saturation curves for the purging steps. After the deposition with the according parameters the samples were measured with SE. The average values for one deposition were entered into the graphs below and a fitting curve was modeled. The according fitting functions and parameters can be seen in Table 5.

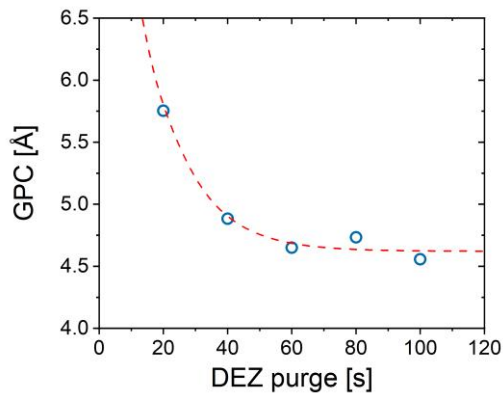


Figure 18: DEZ purge saturation curve

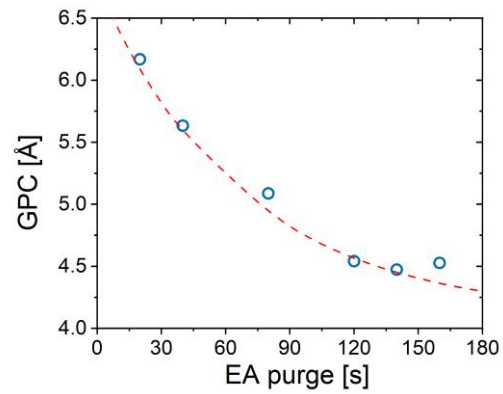


Figure 19: EA purge saturation curve

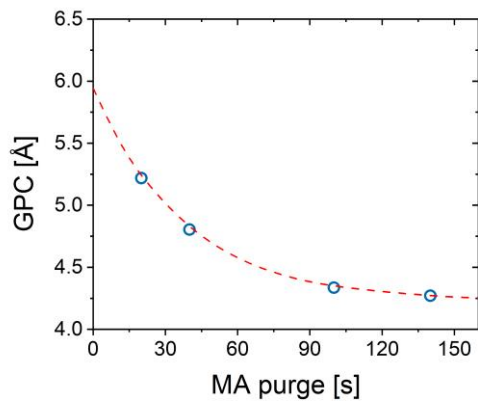


Figure 20: MA purge saturation curve

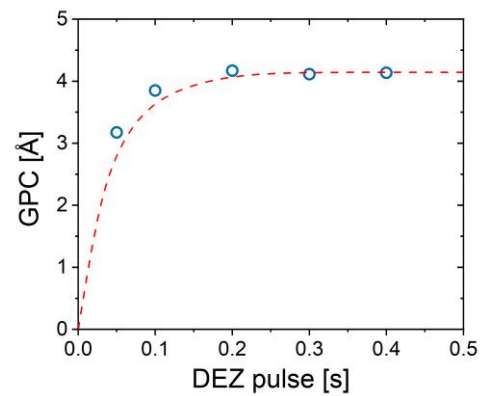


Figure 21: DEZ pulse saturation curve

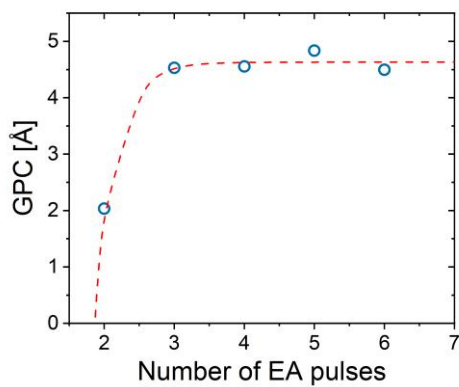


Figure 22: EA pulse saturation curve ( $\hat{a}$  1.5s)

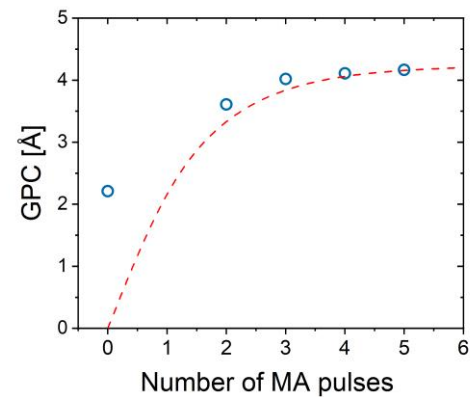


Figure 23: MA pulse saturation curve ( $\hat{a}$  0.1s)

Figure	Fit function	Fit parameter
Figure 18	$GPC_{(t_{purge})} = G + A * e^{(-C_1 * t_{purge})}$	$G = 4.62 \text{ \AA}, A = 4.95 \text{ \AA}, C_1 = 0.0738 \text{ s}^{-1}$
Figure 19		$G = 4.12 \text{ \AA}, A = 2.65 \text{ \AA}, C_1 = 0.0150 \text{ s}^{-1}$
Figure 20		$G = 4.23 \text{ \AA}, A = 1.71 \text{ \AA}, C_1 = 0.0275 \text{ s}^{-1}$
Figure 21	$GPC_{(t_{exp})} = G * (1 - e^{-C_2 * (t_{exp} - t_0)})$	$G = 4.14 \text{ \AA}, C_2 = 24.593 \text{ s}^{-1}, t_0 = 0$
Figure 22		$G = 4.63 \text{ \AA}, C_2 = 3.1931 \text{ s}^{-1}, t_0 = 1.8189 \text{ s}$
Figure 23		$G = 4.23 \text{ \AA}, C_2 = 0.83063 \text{ s}^{-1}, t_0 = 0$

Table 5: Fitting functions and according parameters of saturation curves

The average of the fitting parameters G yields the GPC in saturation:

$$GPC = 4.3 \frac{\text{\AA}}{\text{cycle}}$$

The ideal deposition recipe for this setup can be determined by choosing the purging and exposure times in a manner that they are in the saturation regime but as short as possible. Therefore the following parameters were found:

Table 6: Optimized parameters for ABC-deposition

$t_{DEZ,exposure}$	$t_{DEZ,purge}$	$n_{EA}$	$t_{EA,purge}$	$n_{MA}$	$t_{MA,purge}$
$0.3 \text{ s}$	$100 \text{ s}$	$4$	$140 \text{ s}$	$4$	$100 \text{ s}$

Due to a lack of DEZ and restrictions because of the corona virus the perfect recipe for the ABC deposition was found but could not be applied for longer depositions. For the saturation curves, depositions of 50 cycles were performed, to have samples with sufficient thickness for the investigation with SE. As for the further proceed (heating and characterization) samples with higher thickness were necessary, some preliminary samples with a slightly different recipe were produced.



## 4.2 THIN FILM CHARACTERISATION

### 4.2.1 Heating Experiments

The heating experiments were carried out for both AB- and ABC-deposited samples. Therefore, the zinc oxide films were heated to 400°C and 600°C with a heating rate of 200°C per hour and cooled back down to room temperature afterwards.

The AB-deposited metal-organic hybrid films had a thickness of approximately 50 nm and the transformation was characterized with the help of in-situ and ex-situ techniques. The samples were heated on the heating stage of the ellipsometer while constantly measuring the development of the thickness and refractive index. FTIR measurements were carried out before and after the heating process to point out the change in the chemical composition. To determine the crystallographic structure of the obtained porous ZnO XRD measurements were performed after heating the sample.

The ABC-deposited zinc oxide films which were produced by following a preliminary recipe reached a thickness of approximately 150 nm. In this case the samples were only characterized by the in situ ellipsometry measurements.

#### 4.2.1.1 *In situ Ellipsometry*

Measuring the refractive index and thickness of a sample during the heating process allowed to depict the different temperature regimes of the transformation mechanisms. Therefore, the ellipsometer (Dev. 14) was equipped with a heating stage (Dev. 15) and with the help of the system controller (Dev. 16) the temperature was regulated.

The software completeEASE was not only used to control the measurement but for fitting. The required temperature ramp can be entered into the software as soon as all required devices are connected.

A model (Si\_Temp\_JAW) for the substrate was found in the library of the software that takes the temperature change into account and adjusts the material properties to it. For the oxide layer the NTVE\_JAW model was used and a Cauchy model was applied for the deposited film.

In the following graphs the refractive index and thickness of a AB-deposited film that was heated to almost 600°C (600°C could not be reached at the maximum temperature of the heating stage) is shown.

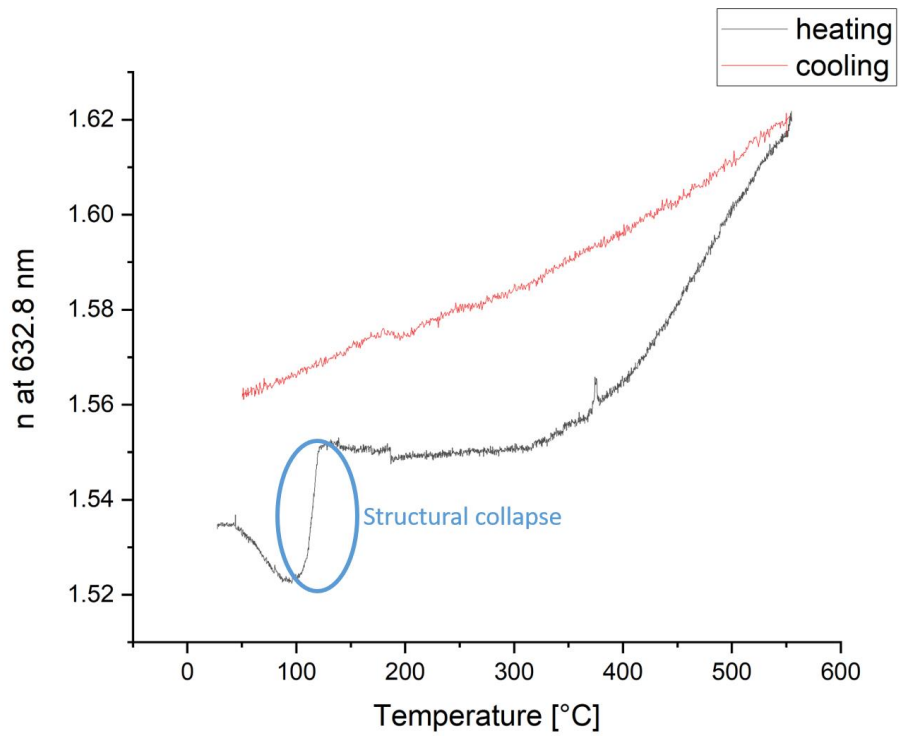


Figure 24: Refractive index at 632.8 nm vs. temperature of AB-sample

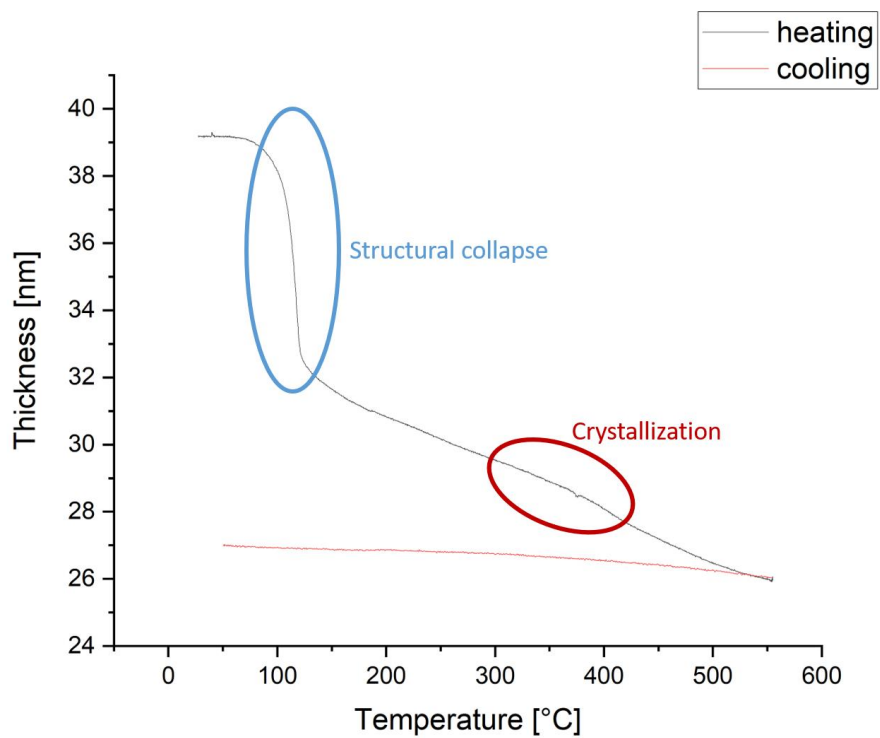


Figure 25: Thickness vs. temperature of AB sample

In Figure 24 and Figure 25 one can easily see the different transformation regimes for the film produced by a AB-deposition with DEZ and EG. At around 100°C the refractive index increases rapidly and at the same time a steep decline in thickness is observed. This indicates the removal of the organic part and therefore a structural collapse of the film. From approximately 120°C to 350°C the refractive index stays mainly constant but the thickness is still decreasing which is primarily attributed to reorientation processes. At around 350°C the slope of the thickness shows a small change and indicates the start of the crystallization regime. Just over 500°C the thickness stabilizes which denotes the termination of the transformation process.

When the sample is cooled down the thickness stays mainly constant and the refractive index decreases. The decrease of the refractive index is a indication of a crystalline ZnO film [23], although the rate is much higher than literature values of dense ZnO.

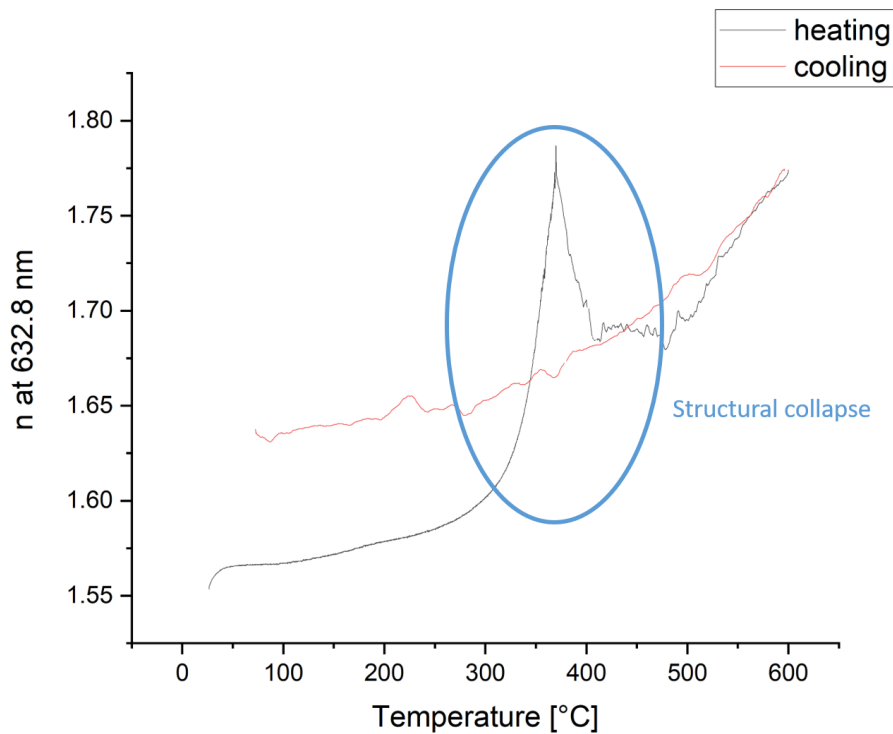


Figure 26: Refractive index at 632.8 nm vs. temperature of ABC-sample

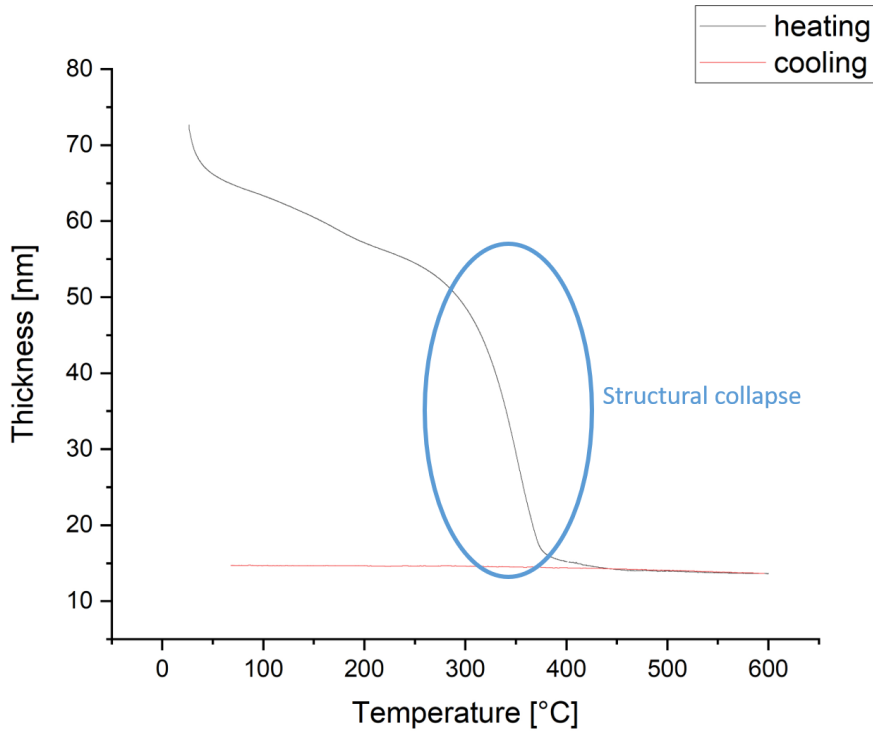


Figure 27: Thickness vs. temperature of ABC-sample

In contrast to the AB-deposited films the thickness of the ABC-deposited samples decreases already from the beginning of the measurement. In the regime from 25°C to roughly 300°C a moderate increase of the refractive index and linearly decline of the thickness is observed. This indicates that the organic content is gradually removed. From 300°C to around 370°C a structural collapse similar to the one in the AB-sample can be observed. In this regime the decrease in the thickness and the increase in the refractive index are very steep. Additionally to the removal of the organic content this regime is also attributed to the crystallization of the ZnO.

At higher temperatures than 370°C the thickness changes are insignificant. The index of refraction though undergoes some unique changes that are not clearly understood. After a steep decrease between 370°C and 400°C the slope of the index of refraction increases again until the final temperature is reached.

Almost no changes in the thickness of the film could be observed while cooling the sample back down to room temperature. Similar to a film deposited with DEZ and EG the refractive index decreases steadily. As already mentioned above this is an indication for crystalline ZnO [23].

#### 4.2.1.2 *Ex Situ FTIR: Before and After Heating*

To check if the organic part could be removed, FTIR measurements (Dev 12) were carried out before and after the sample was heated. With the help of the Opus software the settings for the measurement can be entered. The FTIR was set to measure in the wave number regime between 500 and 4000  $\text{cm}^{-1}$  because the detector becomes unreliable in lower areas. For each measurement 1000 scans were averaged to achieve an adequate signal-to-noise ratio. At the beginning a background measurement of the pure silicon wafer had to be performed. After this the software automatically subtracts the background from each measurement. The graph below is baseline corrected and smoothed.

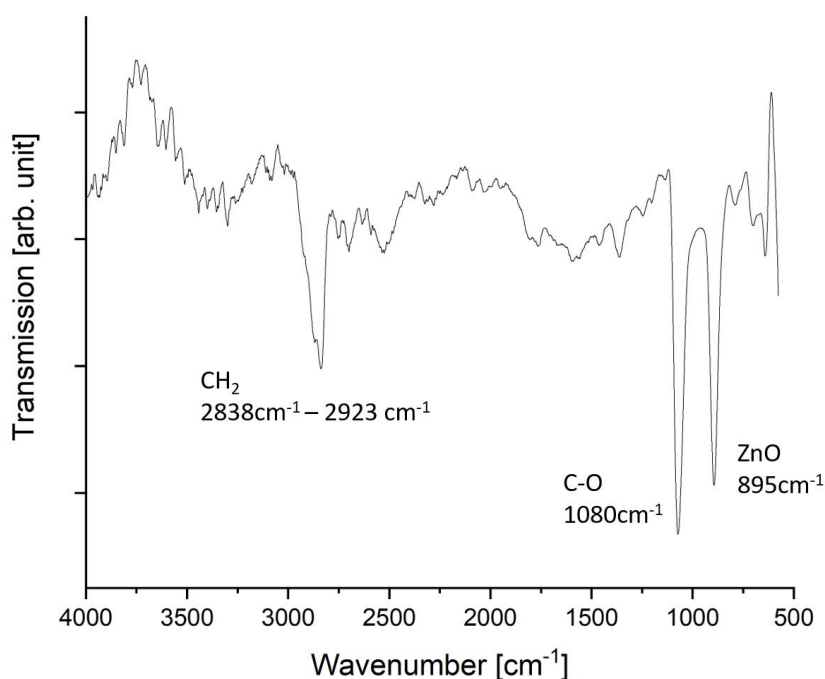


Figure 28: FTIR of AB-zincone film right after deposition

Figure 28 shows the transmission spectrum of an AB zincone film directly after the deposition. The previous work on zincones deposited with DEZ and EG [7] shows the same FTIR results and therefore was used as a reference to assign the peaks. The peaks between 2838 and 2923  $\text{cm}^{-1}$  are C – H stretching modes in a  $\text{CH}_2$  unit. The peak at 1080  $\text{cm}^{-1}$  can be assigned to a C – O mode and the peak at 895  $\text{cm}^{-1}$  is related to a Zn – O stretching mode.

As the FTIR only allows to measure to a wavenumber of 500  $\text{cm}^{-1}$  and the specific peaks for crystalline zinc oxide lay below that the results of the calcinated samples did

not show peaks between 500 and 4000  $\text{cm}^{-1}$ . This is a sign that all the organic content could be removed.

The ABC samples were only measured after the calcination process and as for the AB samples no absorption peaks related to bonds of organic elements could be found.

#### 4.2.1.3 Ex Situ XRD after heating

To analyze the crystallinity of the samples XRD measurements (Dev 13) were executed after the heating process. The X-ray diffractometer (Dev. 13) utilizes a  $\text{CuK}\alpha$  X-ray source with a wavelength of  $\lambda_{\text{CuK}\alpha} = 1.542 \text{ \AA}$ .

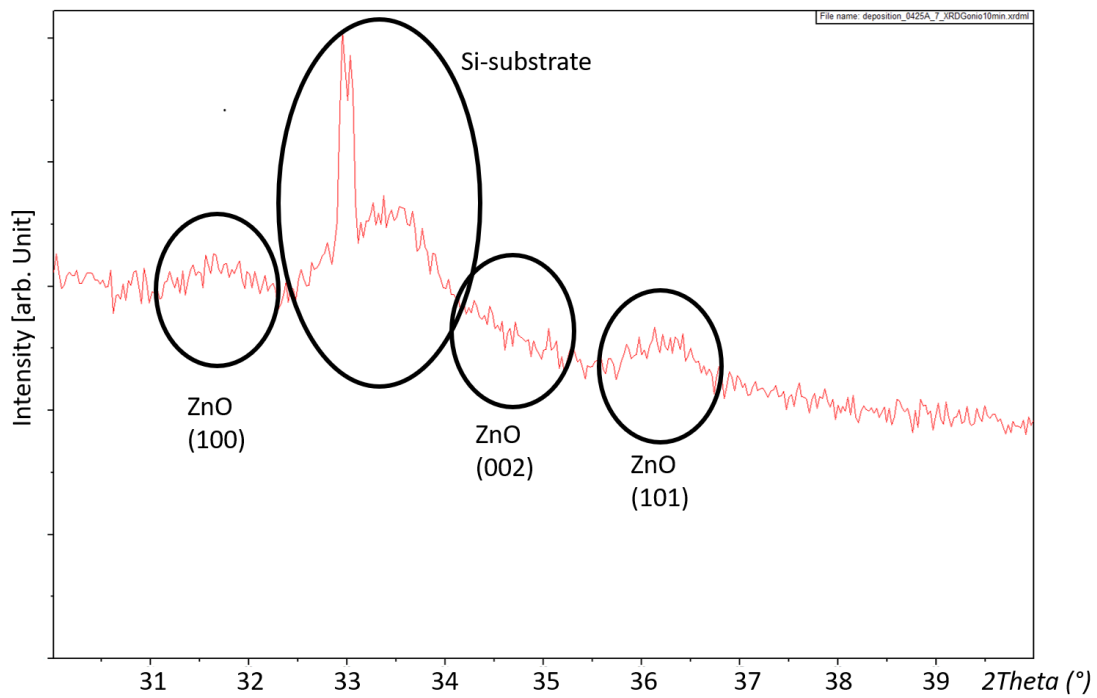


Figure 29: XRD of AB sample heated to 600°C

The XRD measurement shows clearly diffraction peaks that can be assigned to crystalline ZnO. The (100) and (101) net planes show characteristic peaks at 31.7° and 36.1° scattering angle, respectively. At 34.3° a small peak, assigned to diffraction at (002) ZnO net planes, can be spotted.

## 4.2.2 Plasma treatment of AB samples

Another method to get rid of the organic content in the samples is the treatment with oxygen plasma. Therefore, a direct plasma reactor with a shower-head electrode is used. The top electrode is connected to a radio frequency power generator and the ground electrode is the reactor bottom, where the sample is placed. Oxygen gas is lead through the shower head into the reactor and oxygen plasma is produced.

To examine the effect of the plasma on the zincone film samples with almost the same initial thickness were treated with oxygen plasma for different time spans between 0 and 60 minutes. The samples were measured with SE before and after the treatment. In the following graph (Figure 30) the evolution of the refractive index and the thickness are depicted as a function of the plasam treatment time.

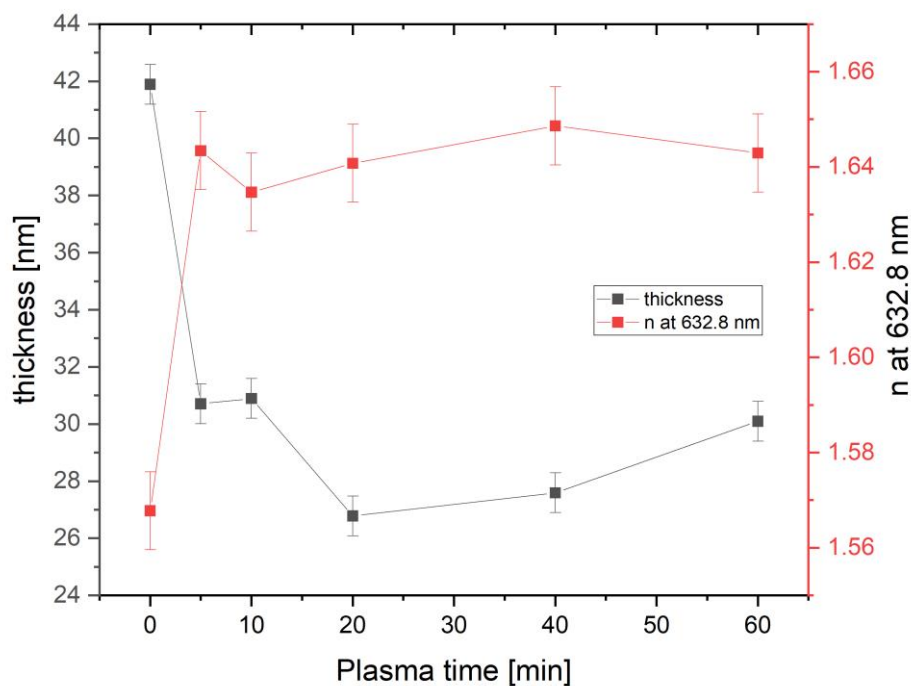


Figure 30: Refractive index and thickness vs. plasma treatment time

The major changes happen in the first 5 minutes. Due to the removing of the organic content the film thickness decreases and the refractive index increases. From 5 to 60 minutes treatment time, the thickness and index of refraction stay almost constant. The error bars in the graph arise from the small differences of the initial thickness and refractive indexes of the different samples.



XRD measurements after the treatment with plasma did not show any peaks as was already assumed and therefore the obtained ZnO was not crystalline. A possible way to get crystalline ZnO would be to heat the sample additionally to the plasma treatment. As there was already an easy possibility investigated to transform the zincone film into a porous crystalline ZnO structure no further attempts in this field were made.

### 4.2.3 Ellipsometric Porosimetry (EP)

With the help of ellipsometric porosimetry the quantity of open porosity could be investigated. As there exists already enough data of EP measurements [7] for AB deposited films only one sample which was heated to 600°C was tested. For the ABC deposited films measurements were carried out for different samples which were heated to 400, 500 and 600°C.

For the EP measurement the stage (Dev. 15) was used again (chapter In situ Ellipsometry). However, to control the humidity surrounding the sample the stage had to be isolated from the environment. Therefore, a special dome with two transparent windows for the light beam of the ellipsometer was fixed on the stage. Two connections on the stage allow the water vapour to flow through the chamber. For a precise control over the relative humidity the construction shown in Figure 31 was used.

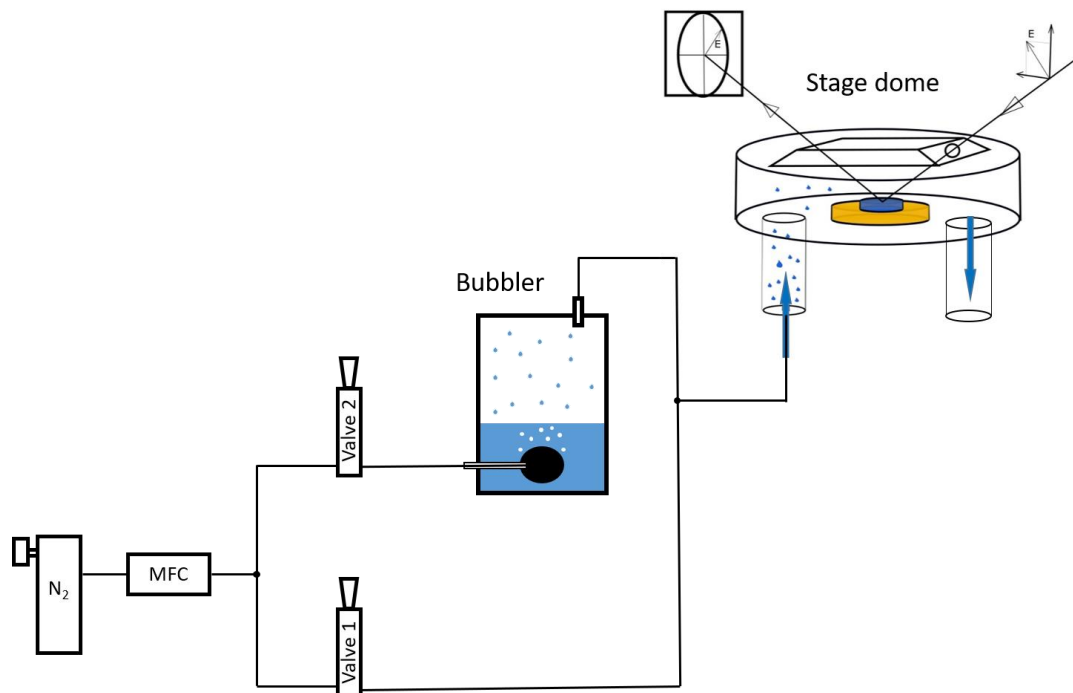


Figure 31: Setup of EP measurement

The flow of Nitrogen gas is controlled by a mechanical mass flow controller (Dev 17) and split into two lines. Both lines are equipped with needle valves (Dev. 18). One valve regulates the amount of  $N_2$  gas that is directly going into the stage, the other valve controls the gas flow through the bubbler. With this apparatus the relative humidity surrounding the sample can be controlled from 0 to almost 100% by only varying the valve positions of the needle valves. A humidity sensor (Dev. 19) is placed inside the dome to record the relative humidity.

#### 4.2.3.1 EP upon Heating AB sample to 600°C

For this EP measurement a sample which was produced with DEZ and EG and thereafter calcinated at 600°C was used. Therefore, the sample was placed into the ellipsometer stage together with the humidity sensor and the chamber was shut with the special dome. The humidity was increased in 5% steps from 0 to around 85% and the index of refraction and the thickness was measured constantly. When the humidity stayed constant at a step the measured values were noted. The relative humidity could not be further increased than 85% due to restrictions of the experimental setup.

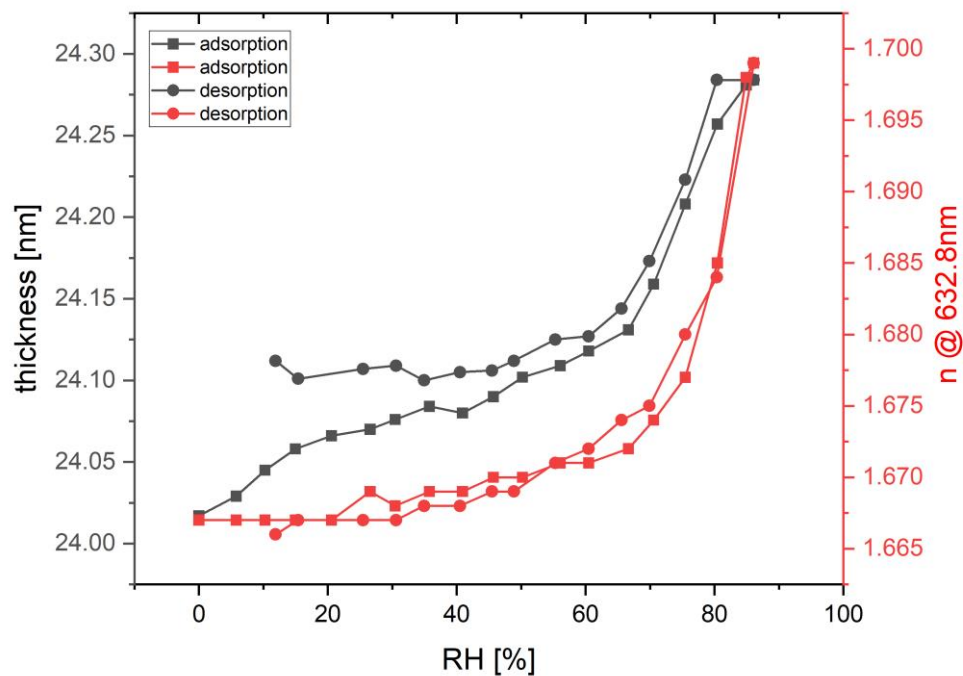


Figure 32: Thickness and refractive index vs. relative humidity of AB-sample heated to 600°C

In Figure 32 one can see the increasing refractive index when more and more water is adsorbed. For the desorption the index of refraction follows the line of the adsorption quite well and stops again at the initial value. The thickness swells around 1% when the water is adsorbed and it doesn't return to its initial value. However the difference between initial and final value is less than 0.1 nm and can be attributed to inaccuracies in the measurement.

Using Equation 8 the volume fraction of adsorbed water in the open pores is calculated. As the maximum humidity was reached with the setup by only 85% two more datapoints at 90 and 95% were added by extrapolating the data.

In Figure 33 the volume fraction is shown for the adsorption regime. The maximum is reached around 11 % which represents the amount of open porosity for this film. In a previous work [7] a porosity between 12 and 13% was measured for a similar film.

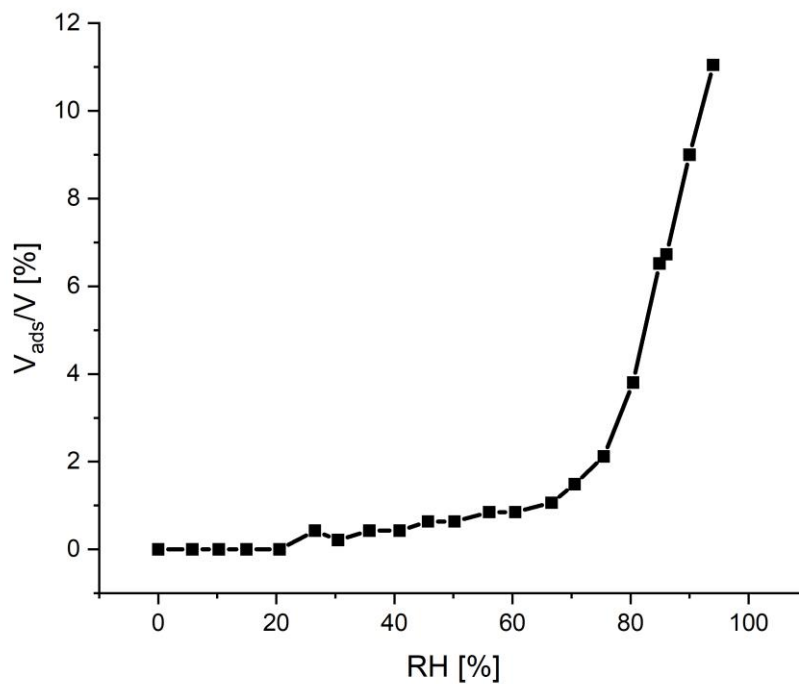


Figure 33: Volume fraction of adsorbed water vs. humidity in AB film

For the pore size distribution the maximum radius of filled pores has to be calculated with the help of Equation 10. Thereafter, the cumulative volume fraction can be related to their maximum radius. By taking the derivative shown in Equation 1, the pore size distribution is obtained. The Kelvin equation is not valid for a pore radius smaller than one nanometer and therefore the PSD was only calculated for larger pore radii.

The pore size distribution in Figure 34 shows a maximum at  $r_{pore} = 2.2$  nm.

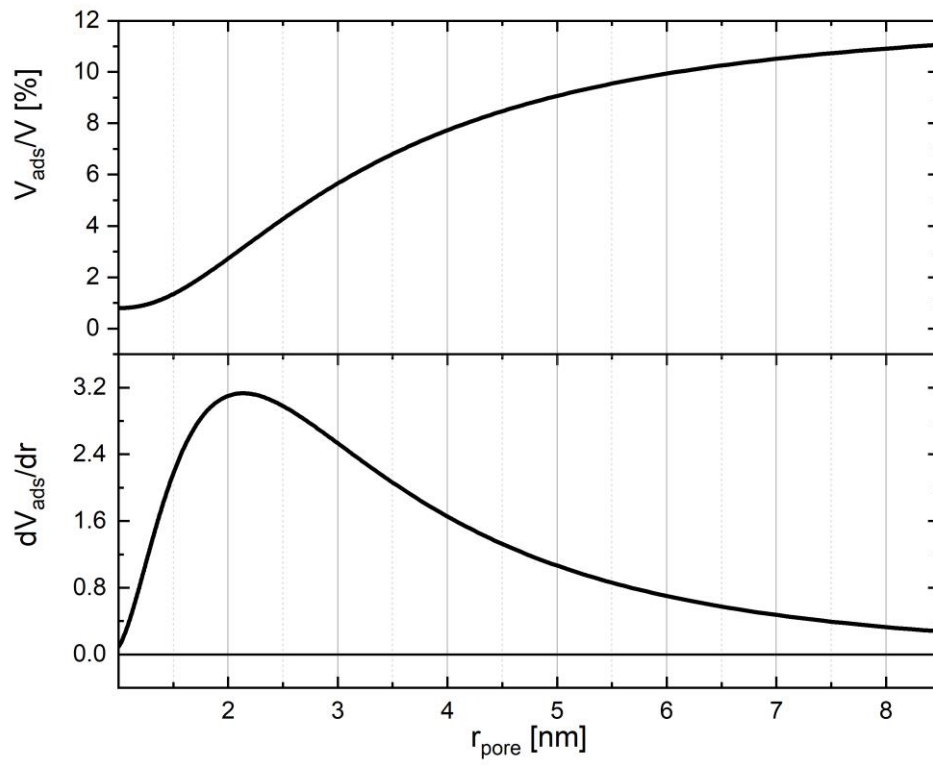


Figure 34: PSD of AB sample

#### 4.2.3.2 EP upon Heating ABC sample to 400, 500 and 600°C

The samples which were produced with DEZ, EA and MA were heated to 400, 500 and 600°C. After the calcination an ellipsometric porosimetry measurement like above was performed for all three samples. Though the humidity was not increased stepwise but continuous as a different in-house written program for reading out the relative humidity was available. Therefore, the graphs below show much more data points and were fitted with a polynomial fit.

In the Figure 35, Figure 36 and Figure 37 the thickness (left) and the refractive index (right) are plotted as function of the relative humidity.

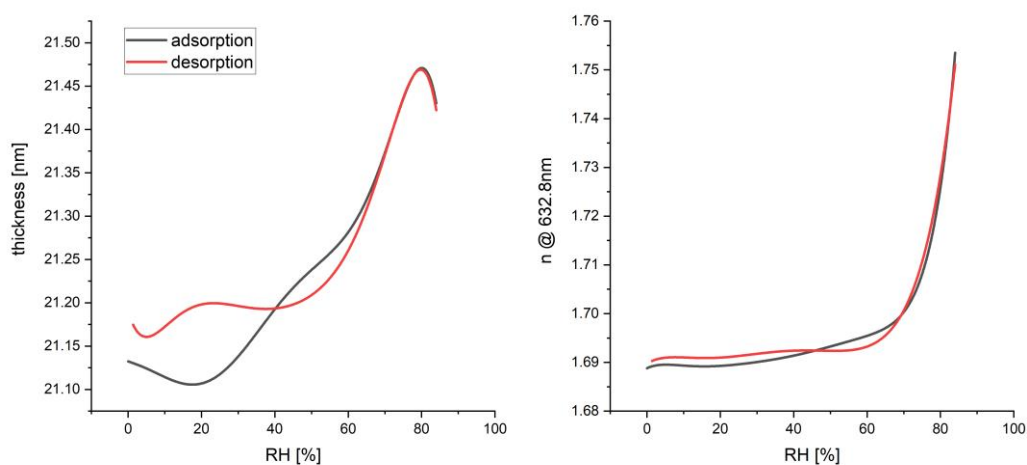


Figure 35: thickness and refractive index vs. relative humidity of 400°C ABC sample

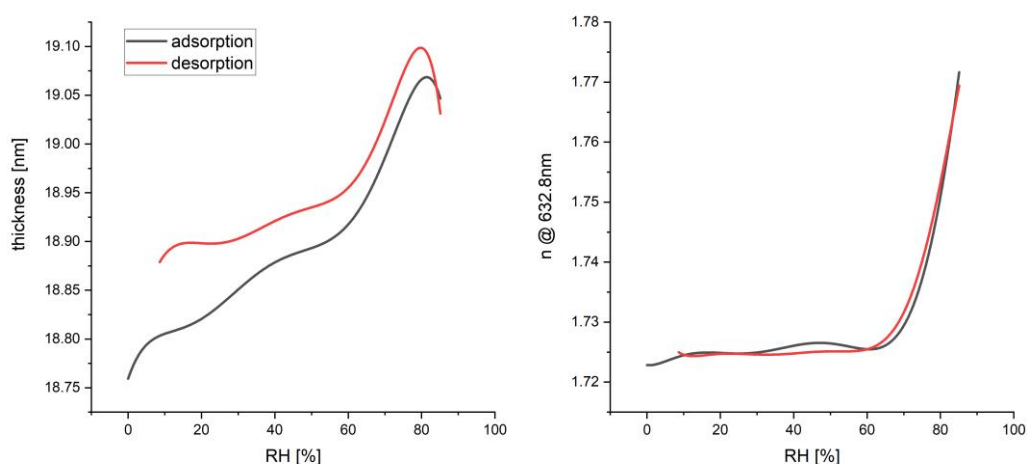


Figure 36: thickness and refractive index vs. relative humidity of 500°C sample

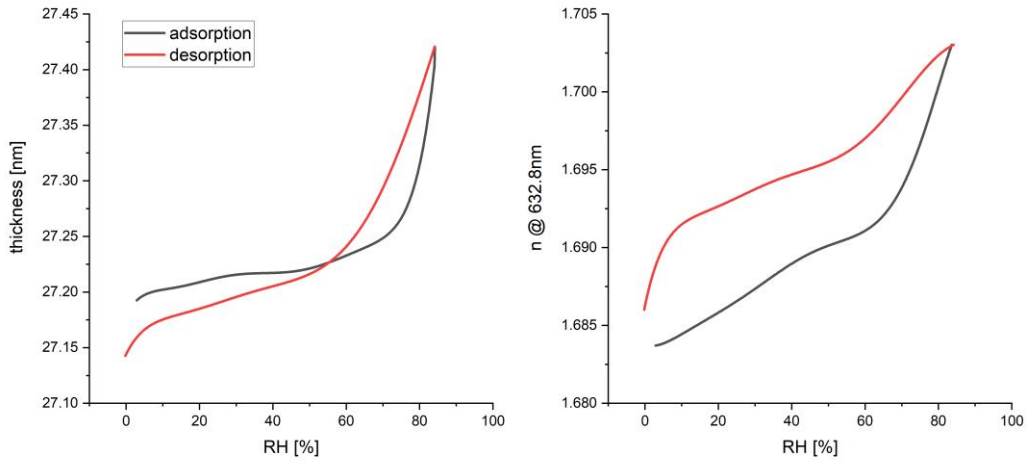


Figure 37: thickness and refractive index vs. relative humidity of 600°C sample

The figures above show that the ABC deposited films swell in a similar manner as the AB films and the increase in thickness lays below 0.4 nm. The refractive index of the differently heated samples all return to the initial values after adsorbing and desorbing the water vapour. This indicates that the samples are stable in water.

Similar to the AB sample the volume fraction of adsorbed water and the pore size distribution was calculated for the differently heated ABC samples (Figure 38 & Figure 39).

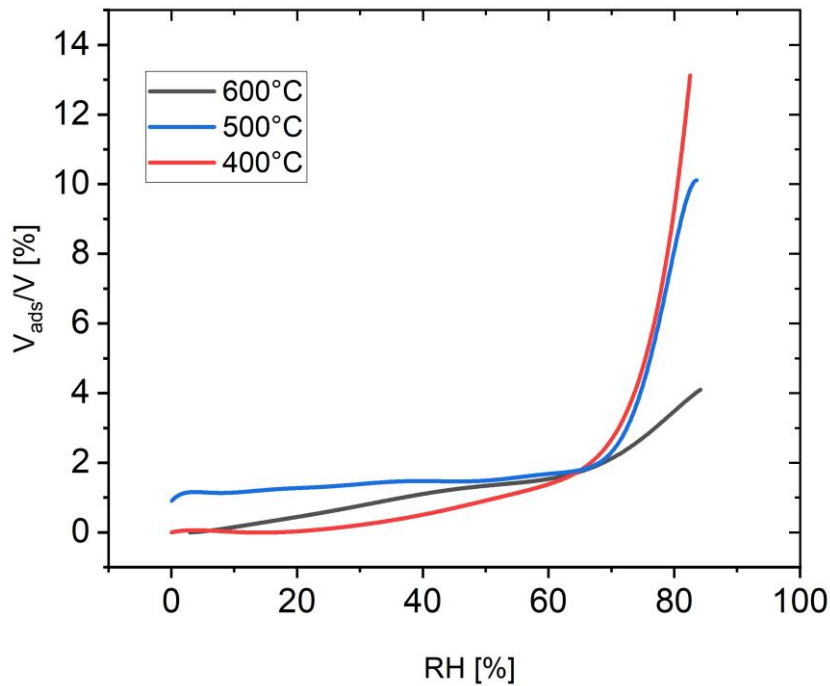


Figure 38: Volume fraction of adsorbed water vs. humidity in ABC film

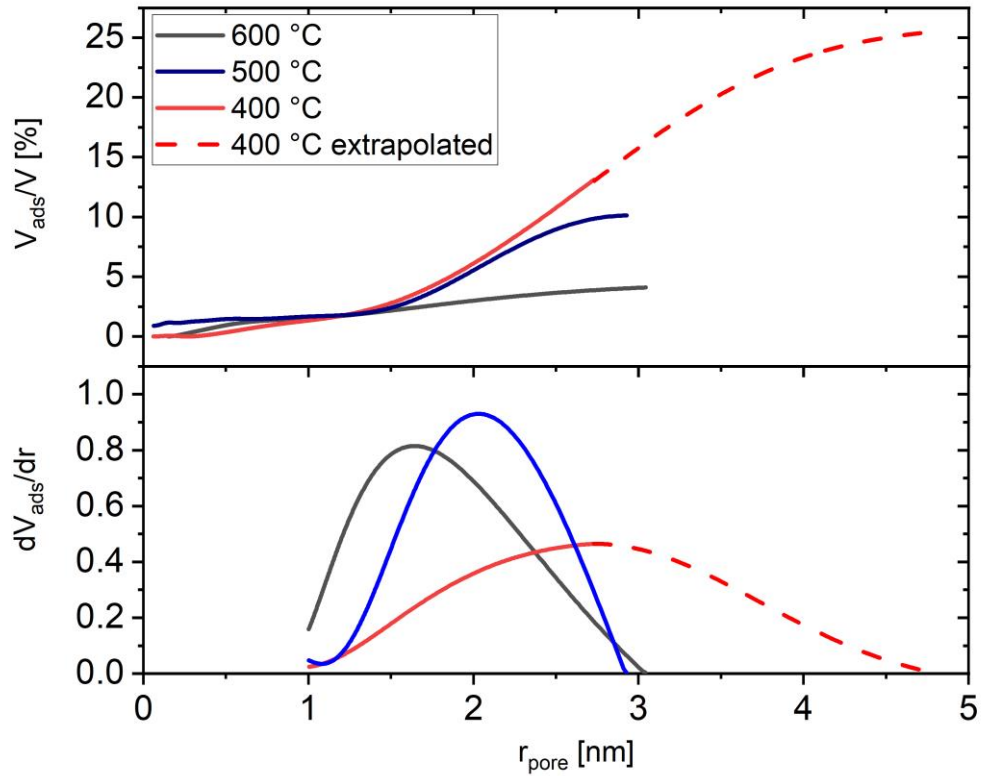


Figure 39: PSD of ABC samples

In Figure 38 one can clearly see the effect of the calcination temperature on the volume fraction of water in the pores at a specific relative humidity. The maximum and therefore the value of open porosity is the largest for the sample which was heated to 400°C.

Figure 39 shows that the largest average pore radius is achieved for the sample that was calcinated at the lowest temperature 400°C. The according values calculated from the PSD for pore radii over 1 nm are 2.8, 2, and 1.8 nm for the thinfilms that were heated to 400, 500 and 600°C, respectively. The pore size distribution of the 400°C sample was extrapolated (dashed red line) for radii larger than 3 nm. Therefore a gaussian behavior was assumed because comparable PSDs show symmetric or right-skewed behaviour [7]. By integrating this part the cumulative distribution could be extrapolated too.



#### 4.2.4 Photocatalytic test

A practical test was carried out in the course of this work to show if the porosity of the ZnO samples enhances the photocatalytic reactivity. Therefore, the degradation of a methylene blue dye is measured. The chemical reactions for this can be seen in the chapter Photocatalytic Test.

For this test methylene blue (MB) with a molar weight of 319.85 g/mol and a dye content greater or equal than 82% (Sigma Aldrich) was used. The powder was diluted with ionized water to a  $1 \cdot 10^{-6}$  molar solution. A sample of this solution was filled into a cuvette and the absorbance at 664nm was measured with the UV-VIS spectrophotometer (Dev 20). A blank test (irradiated solution without sample) and a dark test (solution with sample but not irradiated) was carried out simultaneously with the real test. This should proof the reliability of the test.

Therefore, three glass beakers were filled with the solution and in two of them calcinated AB samples were placed. One of the sample containing beakers was wrapped up with aluminum foil to keep it dark. The two remaining beakers, one blank and one with a sample, were placed under a UV-lamp (Dev 21).

The variation in the concentration of the methylene blue as a function of the irradiation time was measured spectrophotometrically by sampling the solutions of all three beakers. After the measurement of the solution's absorbance at 664nm the sample was returned. Thereafter the solutions were stirred. The irradiation process was carried out for two to three hours depending on the reactivity.

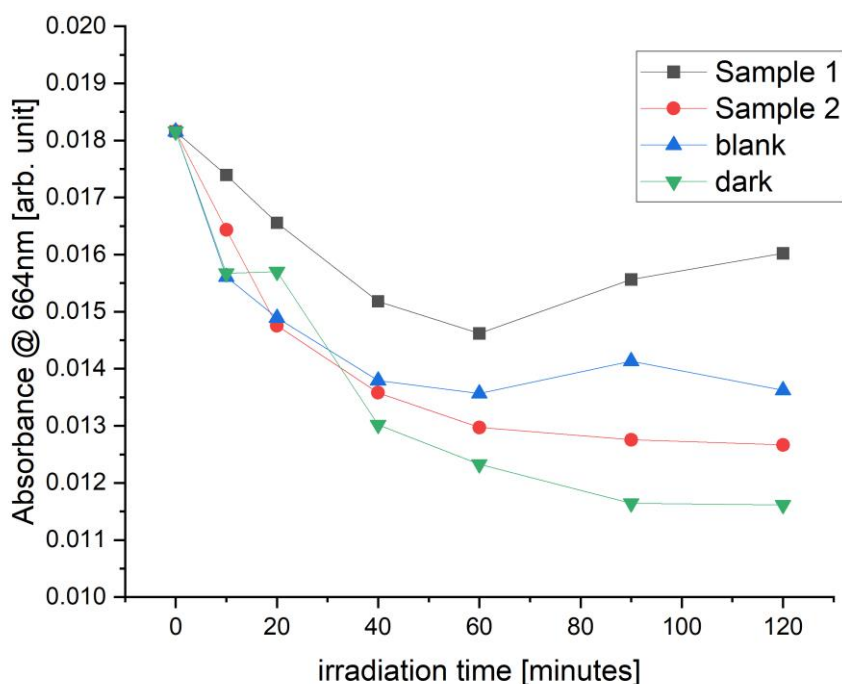


Figure 40: Photocatalytic test 1, absorbance vs. irradiation time

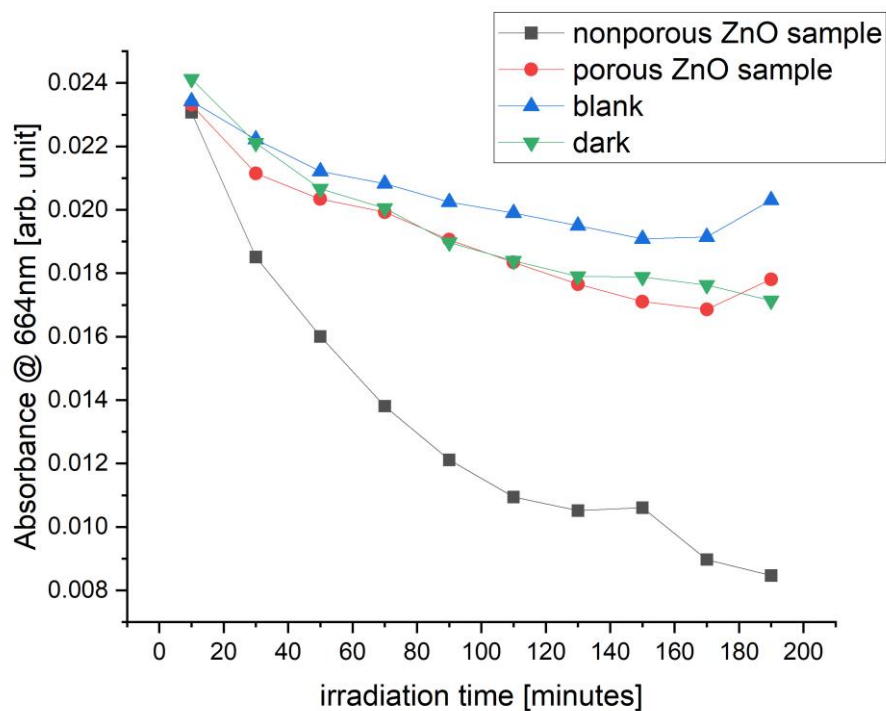


Figure 41: Photocatalytic test 2, absorbance vs. irradiation time

Figure 40 shows the result several tests of the AB samples yielded. After 120 minutes the test was stopped because no photocatalytic effect could be observed. To exclude application errors different factors like the size of the sample and the concentration of MB in the solution were varied but still no degradation was measured.

As it is known that ZnO is photocatalytic active a test with one porous and one non-porous ZnO sample was carried out. In Figure 41 one can clearly see that the non-porous ZnO is photocatalytically bleaching the dye whereas the porous sample is showing no effect.

The reason why a sample with increased surface area is less reactive is not completely understood, yet. Assumptions like clogging of the methylene blue molecules in the pores of the film were not further investigated but might play a role in the process.

#### 4.2.5 Degradation

The stability of the zincone films in ambient air was investigated because they seemed to show a different behaviour than films that were produced in a previous work of Richard Berger [8]. Spectroscopic ellipsometry measurements in  $N_2$  and air environments were performed. Therefore the same sample stage that was used for the ellipsometric porosimetry was applied. Figure 42 shows a SE measurement where the sample was kept in a  $N_2$  environment until minute 20 and then released to the air environment.

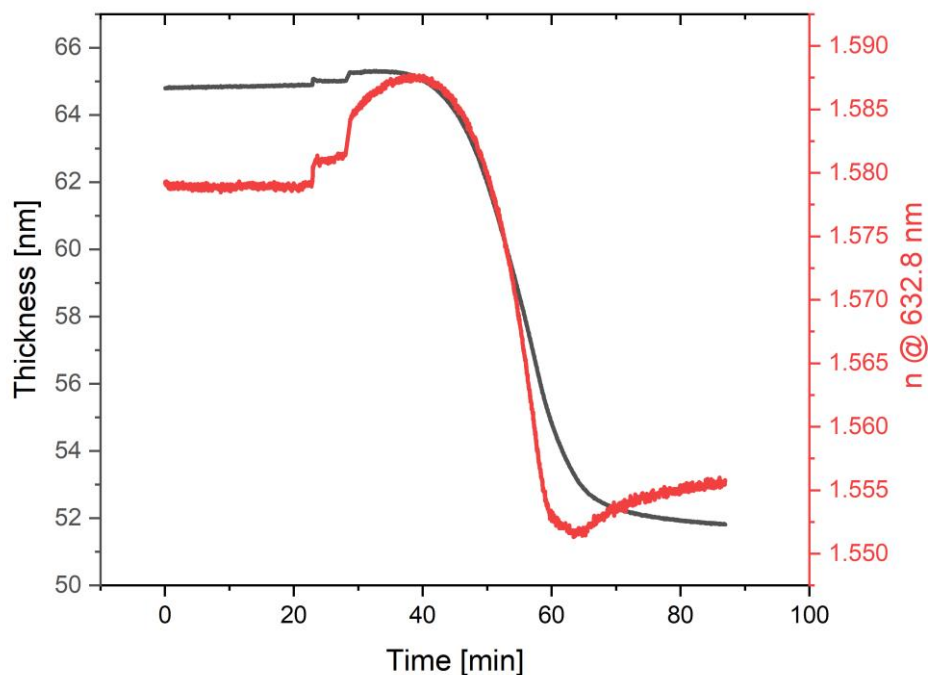


Figure 42: Degradation of zincone in  $N_2$  and air environment

The steps between 20 and 30 minutes are measurement errors caused by the removing of the lid. In the span between 40 and 70 minutes a steep decrease of the thickness and refractive index is recorded and after 70 minutes both values stabilize again. The trend of the curves are similar to the measurements of the previous work [8] but the transformation occurred in a very elongated time span.

The reason of this discrepancy, which manifested itself more and more during this work, is most likely the humidity level of the air. A huge variation in the degradation behaviour of the zincone films was noticed between the seasons. In winter, where the samples of the previous work [8] also were produced, the low humidity level decreased the velocity of the degradation extremely, whereas in summer the process took place in the first minutes to hours.

## 5 SUMMARY AND CONCLUSIONS

---

In the course of this thesis the delivery of two different zincone films via molecular layer deposition was investigated. Starting from the reproduction of a metal-alkoxide film from a previous work [7] by utilizing the precursors diethyl zinc and ethylene glycol and the purgin gas argon, a three step MLD process was introduced. Therefore the organic precursors ethanolamine and maleic anhydrate were employed additionally to the metalorganic precursor DEZ.

An ideal deposition recipe for the three step deposition was found at the following precursor and purging times:

$t_{DEZ,exposure}$	$t_{DEZ,purge}$	$n_{EA}$	$t_{EA,purge}$	$n_{MA}$	$t_{MA,purge}$
<i>0.3 s</i>	<i>100 s</i>	<i>4</i>	<i>140 s</i>	<i>4</i>	<i>100 s</i>

Applying this recipe a constant GPC of  $4.3 \pm 0.2 \text{ \AA}/\text{cycle}$  was measured.

The transformation behaviour of the two differently produced zincone layers, i.e. the modification of the refractive index and the thickness as well as the formation of pores upon heating to different temperatures were investigated with spectroscopic ellipsometry and ellipsometric porosimetry. The results show that the open porosity can be tuned by varying the precursor reactants and the calcination temperature. An open porosity of 25% with an expected average pore radius of 2.8 nm could be calculated for the three step sample which was heated to 400°C. The values for the ABC samples heated to 500°C and 600°C are 10% open porosity with 2 nm average pore radius and 4% with 1.8 nm radius, respectively. The AB sample calcinated at 600°C showed 11% open porosity and 2.2 nm for the average pore radius.

The structural transformation during the heating process measured by SE show that the ABC samples collapse between 300°C and 370°C which can be assigned to the removal of the organic content. At elevated temperatures between 370°C and 600°C the thickness staves constant while the index of refraction undergoes changes that suggest an internal transformation of the film that need to be further investigated. The cooling behaviour is similar to the AB sample indicating the presence of crystalline ZnO after calcination.

By utilizing different precursor molecules in the MLD process it is possible to deliver a conformal ZnO coating with a tunable porosity on textured substrates. Since this approach of synthesizing ZnO is pretty new the limits of the method are not known yet and have to be studied in the future.

## 6 DEVICE LIST

<b>Device</b>	<b>Brand</b>	<b>Type</b>
Dev 1: Rotary vane pump	Pfeifer	DUO 005 M
Dev 2: Heating wire	Winkler	WBG00402230XX400-025000625
Dev 3: Heating disk	Omega	KHR-2/10-P
Dev 4: Reactor and line temperature controller		
Dev 5: Stage temperature controller	Omega	CN142
Dev 6: ALD valve	Swagelok	ALD 3
Dev 7: Purging gas valve	Burkert	6013A 3.0 FKM MS
Dev 8: Mass flow controller	MKS	MF1
Dev 9: Microcontroller	Arduino	Uno
Dev 10: Communication module	MKS	AS11870G-02
Dev 11: Pressure gauge	Inficon	MPG400
Dev 12: FTIR		
Dev 13: X-Ray diffractometer	BOMEM	MB-102
Dev 14: Ellipsometer	J. A. Woolam Co.	M-2000V
Dev 15: Ellipsometer temperature controller stage with an additional dome	Linkam	THMS600
Dev 16: Link Pad System Controller	Linkam	T95
Dev 17: Mechanical mass flow controller	KROHNE	DK800/PV
Dev 18: Needle valve	Swagelok	SS-4BMW
Dev 19: Humidity and temperature sensor	Sparkfun	SHT15
Dev 20: UV-VIS Spectrophotometer	Shimadzu	UV-1800
Dev 21: UV-lamp	Vilber Lourmat	VL-6.L

## 7 FIGURE LIST

---

Figure 1: Precursor structural formulas.....	3
Figure 2: Scheme of two step reaction sequence using (A) Diethylzinc (DEZ) and (B) Ethylene glycol (EG).....	4
Figure 3: Scheme of three step reaction sequence using (A) diethylzinc (DEZ), (B) ethanolamine (EA) and (C) maleic anhydride (MA). ....	5
Figure 4: Saturation curves.....	6
Figure 5: Zincone film deposited with DEZ and EG.....	10
Figure 6: (A) tilted molecules, (B) double reaction, (C) passivation reaction with water .....	11
Figure 7: Zincone film deposited with DEZ, EA and MA .....	12
Figure 8: (A) forming of maleimide ring, (B) passivating reaction with water.....	12
Figure 9: Scheme of the production of porous ZnO with different organic molecules	13
Figure 10: Scheme of photocatalytic test .....	14
Figure 11: Schematic setup of Michelson interferometer.....	15
Figure 12: Schematic representation of bragg equation .....	17
Figure 13: Ellipsometric porosimetry measurement principle, (scheme reprinted with consent of author [8]).....	20
Figure 14: Scheme of the MLD system .....	23
Figure 15: Left: Scheme of heating circuits (rectangle are heating wires, circle is heating disk) and right: picture of isolated system. ....	24
Figure 16: Cutout of saturation curves (reprinted with consent of author [8]) .....	30
Figure 17: Sample of Ellipsometry measurement .....	31
Figure 18: DEZ purge saturation curve.....	33
Figure 19: EA purge saturation curve .....	33
Figure 20: MA purge saturation curve.....	33
Figure 21: DEZ pulse saturation curve.....	33
Figure 22: EA pulse saturation curve ( $\lambda$ 1.5s) .....	33
Figure 23: MA pulse saturation curve ( $\lambda$ 0.1s) .....	33
Figure 24: Refractive index at 632.8 nm vs. temperature of AB-sample .....	36
Figure 25: Thickness vs. temperature of AB sample.....	36
Figure 26: Refractive index at 632.8 nm vs. temperature of ABC-sample .....	37
Figure 27: Thickness vs. temperature of ABC-sample .....	38
Figure 28: FTIR of AB-zincone film right after deposition.....	39
Figure 29: XRD of AB sample heated to 600°C .....	41
Figure 30: Refractive index and thickness vs. plasma treatment time .....	42
Figure 31: Setup of EP measurement .....	44
Figure 32: Thickness and refractive index vs. relative humidity of AB-sample heated to 600°C .....	45
Figure 33: Volume fraction of adsorbed water vs. humidity in AB film .....	46
Figure 34: PSD of AB sample.....	47
Figure 35: thickness and refractive index vs. relative humidity of 400°C ABC sample .....	48

Figure 36: thickness and refractive index vs. relative humidity of 500°C sample ....	48
Figure 37: thickness and refractive index vs. relative humidity of 600°C sample ....	49
Figure 38: Volume fraction of adsorbed water vs. humidity in ABC film .....	49
Figure 39: PSD of ABC samples .....	50
Figure 40: Photocatalytic test 1, absorbance vs. irradiation time .....	51
Figure 41: Photocatalytic test 2, absorbance vs. irradiation time .....	52
Figure 42: Degradation of zincone in N <sub>2</sub> and air environment.....	53

## 8 TABLE LIST

---

Table 1: Temperatures of the different parts for AB- and ABC- deposition (colors correspond to Figure 15).....	25
Table 2: Process steps for AB-deposition .....	29
Table 3: Optimized parameters of AB-deposition.....	30
Table 4: Process steps for ABC deposition.....	32
Table 5: Fitting functions and according parameters of saturation curves .....	34
Table 6: Optimized parameters for ABC-deposition.....	34



## 9 BIBLIOGRAPHY

---

### Literaturverzeichnis

- [1] *Porous Zinc Oxide Thin Films: Synthesis Approaches and Applications*. In: *Coatings* 8 (2018), Nr. 2, S. 67
- [2] SINGH, S. P. ; ARYA, Sunil K. ; PANDEY, Pratibha ; MALHOTRA, B. D. ; SAHA, Shibu ; SREENIVAS, K. ; GUPTA, Vinay: *Cholesterol biosensor based on rf sputtered zinc oxide nanoporous thin film*. In: *Applied Physics Letters* 91 (2007), Nr. 6, S. 63901
- [3] DIKICI, Tuncay: *Temperature-dependent growth of ZnO structures by thermal oxidation of Zn coatings electrodeposited on steel substrates and their photocatalytic activities*. In: *Ceramics International* 43 (2017), Nr. 11, S. 8289–8293
- [4] HAN, Byung Suh ; CALISKAN, Salim ; SOHN, Woonbae ; KIM, Miyoung ; LEE, Jung-Kun ; JANG, Ho Won: *Room Temperature Deposition of Crystalline Nanoporous ZnO Nanostructures for Direct Use as Flexible DSSC Photoanode*. In: *Nanoscale research letters* 11 (2016), Nr. 1, S. 221
- [5] YOON, Byunghoon ; SEGHEDE, Dragos ; CAVANAGH, Andrew S. ; GEORGE, Steven M.: *Molecular Layer Deposition of Hybrid Organic–Inorganic Alucone Polymer Films Using a Three-Step ABC Reaction Sequence*. In: *Chemistry of Materials* 21 (2009), Nr. 22, S. 5365–5374
- [6] GEORGE, Steven M. ; LEE, Byoung H. ; YOON, Byunghoon ; ABDULAGATOV, Aziz I. ; HALL, Robert A.: *Metalcones: hybrid organic-inorganic films fabricated using atomic and molecular layer deposition techniques*. In: *Journal of nanoscience and nanotechnology* 11 (2011), Nr. 9, S. 7948–7955
- [7] PERROTTA, Alberto ; BERGER, Richard ; MURALTER, Fabian ; COCLITE, Anna Maria: *Mesoporous ZnO thin films obtained from molecular layer deposited "zincones"*. In: *Dalton Transactions* 48 (2019), Nr. 37, S. 14178–14188
- [8] RICHARD BERGER, BSc: *Nano-Porous Zinc Oxide via Molecular Layer Deposition*
- [9] BROWN, Joseph J. ; HALL, Robert A. ; KLADITIS, Paul E. ; GEORGE, Steven M. ; BRIGHT, Victor M.: *Molecular layer deposition on carbon nanotubes*. In: *ACS nano* 7 (2013), Nr. 9, S. 7812–7823
- [10] CHO, Sangho ; HAN, Gibok ; KIM, Kwan ; SUNG, Myung M.: *High-performance two-dimensional polydiacetylene with a hybrid inorganic-organic structure*. In: *Angewandte Chemie (International ed. in English)* 50 (2011), Nr. 12, S. 2742–2746

- [11] YOON, Byunghoon ; LEE, Younghee ; DERK, Alan ; MUSGRAVE, Charles ; GEORGE, Steven: Molecular Layer Deposition of Conductive Hybrid Organic-Inorganic Thin Films Using Diethylzinc and Hydroquinone. In: ECS, 2011 (ECS Transactions), S. 191–195
- [12] SOOD, Anjali ; SUNDBERG, Pia ; KARPPINEN, Maarit: *ALD/MLD of novel layer-engineered Zn-based inorganic-organic hybrid thin films using heterobifunctional 4-aminophenol as an organic precursor*. In: *Dalton Transactions* 42 (2013), Nr. 11, S. 3869–3875
- [13] SUNDBERG, Pia ; KARPPINEN, Maarit: *Organic and inorganic-organic thin film structures by molecular layer deposition: A review*. In: *Beilstein journal of nanotechnology* 5 (2014), S. 1104–1136
- [14] PENG, Qing ; GONG, Bo ; VANGUNDY, Ryan M. ; PARSONS, Gregory N.: *“Zincone” Zinc Oxide–Organic Hybrid Polymer Thin Films Formed by Molecular Layer Deposition*. In: *Chemistry of Materials* 21 (2009), Nr. 5, S. 820–830
- [15] YOON, Byunghoon ; O'PATCHEN, Jennifer L. ; SEGHETE, Dragos ; CAVANAGH, Andrew S. ; GEORGE, Steven M.: *Molecular Layer Deposition of Hybrid Organic-Inorganic Polymer Films using Diethylzinc and Ethylene Glycol*. In: *Chemical Vapor Deposition* 15 (2009), 4-6, S. 112–121
- [16] LIANG, Xinhua ; JIANG, Ying-Bing ; WEIMER, Alan W.: *Nanocoating zinc alkoxide (zincone) hybrid polymer films on particles using a fluidized bed reactor*. In: *Journal of Vacuum Science & Technology A: Vacuum, Surfaces, and Films* 30 (2012), Nr. 1, 01A108
- [17] LEE, Kian Mun ; LAI, Chin Wei ; NGAI, Koh Sing ; JUAN, Joon Ching: *Recent developments of zinc oxide based photocatalyst in water treatment technology: A review*. In: *Water research* 88 (2016), S. 428–448
- [18] JONGNAVAKIT, P. ; AMORNPITOKSUK, P. ; SUWANBOON, S. ; NDIEGE, N.: *Preparation and photocatalytic activity of Cu-doped ZnO thin films prepared by the sol–gel method*. In: *Applied Surface Science* 258 (2012), Nr. 20, S. 8192–8198
- [19] CHIU, W. S. ; KHIEW, P. S. ; CLOKE, M. ; ISA, D. ; TAN, T. K. ; RADIMAN, S. ; ABD-SHUKOR, R. ; HAMID, M. Abd.A. ; HUANG, N. M. ; LIM, H. N.: *Photocatalytic study of two-dimensional ZnO nanopellets in the decomposition of methylene blue*. In: *Chemical Engineering Journal* 158 (2010), Nr. 2, S. 345–352
- [20] GROSS, Rudolf ; MARX, Achim: *Festkörperphysik*. München : Oldenbourg, 2012 (Mathematik, Physik 10-2012)
- [21] DENDOOVEN, Jolien ; DEVLOO-CASIER, Kilian ; LEVRAU, Elisabeth ; VAN HOVE, Robbert ; SREE, Sreeprasanth Pulinthanathu ; BAKLANOV, Mikhail R. ; MARTENS, Johan A. ; DETAVERNIER, Christophe: *In situ monitoring of atomic layer deposition in nanoporous thin films using ellipsometric porosimetry*. In: *Langmuir : the ACS journal of surfaces and colloids* 28 (2012), Nr. 8, S. 3852–3859
- [22] PFEIFFER VACUUM: *The Vacuum Technology Book Bolume II*

[23] SAHA, Shibu ; MEHAN, Navina ; SREENIVAS, K. ; GUPTA, Vinay: *Temperature dependent optical properties of (002) oriented ZnO thin film using surface plasmon resonance*. In: *Applied Physics Letters* 95 (2009), Nr. 7, S. 71106